TOI-2525 b and c: A pair of massive warm giant planets with strong transit timing variations revealed by TESS

Trifonov, T.; Brahm, R.; Jordán, A.; Hartogh, C.; Henning, T.; Hobson, M.J.; ... ; Winn, J.N.

The Astronomical Journal, 165:179 (23pp), 2023 April https://doi.org/10.3847/1538-3881/acba9b

TOI-2525 b and c: A Pair of Massive Warm Giant Planets with Strong Transit Timing Variations Revealed by TESS*

Trifon Trifonov[1,2], Rafael Brahm[3,4,5], Andrés Jordán[3,4,5], Christian Hartogh[6], Thomas Henning[1], Melissa J. Hobson[1,4], Martin Schlecker[1,7], Saburo Howard[8], Finja Reichardt[1], Nestor Espinoza[9], Man Hoi Lee[10,11], David Nesvorny[12], Felipe I. Rojas[4,13], Khalid Barkaoui[14,15,16], Diana Kossakowski[1], Gavin Boyle[17,18], Stefan Dreizler[6], Martin Kürster[1], René Heller[19], Tristan Guillot[8], Amaury H. M. J. Triaud[20], Lyu Abe[8], Abdelkrim Agabi[8], Philippe Bendjoya[8], Nicolas Crouzet[21], Georgina Dransfield[19], Thomas Gasparetto[22], Maximilian N. Günther[23], Wenceslas Marie-Sainte[24], Djamel Mékarnia[8], Olga Suarez[8], Johanna Teske[25], R. Paul Butler[25], Jeffrey D. Crane[26], Stephen Shectman[26], George R. Ricker[27], Avi Shporer[27], Roland Vanderspek[27], Jon M. Jenkins[28], Bill Wohler[28,29], Karen A. Collins[30], Kevin I. Collins[31], David R. Ciardi[32], Thomas Barclay[33,34], Ismael Mireles[35], Sara Seager[27,36,37], and Joshua N. Winn[38]

[1] Max-Planck-Institut für Astronomie, Königstuhl 17, D-69117 Heidelberg, Germany; trifonov@mpia.de
[2] Department of Astronomy, Sofia University "St. Kliment Ohridski", 5 James Bourchier Boulevard, BG-1164 Sofia, Bulgaria
[3] Facultad de Ingeniera y Ciencias, Universidad Adolfo Ibáñez, Av. Diagonal las Torres 2640, Peñalolén, Santiago, Chile
[4] Millennium Institute for Astrophysics, Chile
[5] Data Observatory Foundation, Chile
[6] Institut für Astrophysik und Geophysik, Friedrich-Hund-Platz 1, D-37077 Göttingen, Germany
[7] Department of Astronomy/Steward Observatory, The University of Arizona, 933 North Cherry Avenue, Tucson, AZ 85721, USA
[8] Université Côte d'Azur, Observatoire de la Côte d'Azur, CNRS, Laboratoire Lagrange, Bd de l'Observatoire, CS 34229, F-06304 Nice cedex 4, France
[9] Space Telescope Science Institute, 3700 San Martin Drive, Baltimore, MD 21218, USA
[10] Department of Earth Sciences, The University of Hong Kong, Pokfulam Road, Hong Kong
[11] Department of Physics, The University of Hong Kong, Pokfulman Road, Hong Kong
[12] Department of Space Studies, Southwest Research Institute, 1050 Walnut Street, Suite 300, Boulder, CO 80302, USA
[13] Instituto de Astrofísica, Facultad de Física, Pontificia Universidad Católica de Chile, Chile
[14] Astrobiology Research Unit, Université de Liège, Allée du 6 Août 19C, B-4000 Liège, Belgium
[15] Department of Earth, Atmospheric and Planetary Science, Massachusetts Institute of Technology, 77 Massachusetts Avenue, Cambridge, MA 02139, USA
[16] Instituto de Astrofísica de Canarias (IAC), Calle Vía Láctea s/n, E-38200, La Laguna, Tenerife, Spain
[17] El Sauce Observatory—Obstech, Chile
[18] Cavendish Laboratory, JJ Thomson Avenue, Cambridge, CB3 0HE, UK
[19] Max Planck Institute for Solar System Research, Justus-von-Liebig-Weg 3, D-37077 Göttingen, Germany
[20] School of Physics & Astronomy, University of Birmingham, Edgbaston, Birmingham, B15 2TT, UK
[21] Leiden Observatory, Leiden University, Postbus 9513, 2300 RA Leiden, The Netherlands
[22] Institute of Polar Sciences—CNR, via Torino, 155-30172 Venice-Mestre, Italy
[23] European Space Agency (ESA), European Space Research and Technology Centre (ESTEC), Keplerlaan 1, 2201 AZ Noordwijk, The Netherlands [39]
[24] Concordia Station, IPEV/PNRA, Antarctica
[25] Carnegie Institution for Science, Earth & Planets Laboratory, 5241 Broad Branch Road NW, Washington, DC 20015, USA
[26] The Observatories of the Carnegie Institution for Science, 813 Santa Barbara Street, Pasadena, CA 91101, USA
[27] Department of Physics and Kavli Institute for Astrophysics and Space Research, Massachusetts Institute of Technology, Cambridge, MA 02139, USA
[28] NASA Ames Research Center, Moffett Field, CA 94035, USA
[29] SETI Institute, Mountain View, CA 94043, USA
[30] Center for Astrophysics | Harvard & Smithsonian, 60 Garden Street, Cambridge, MA 02138, USA
[31] George Mason University, 4400 University Drive, Fairfax, VA 22030, USA
[32] Caltech/IPAC-NASA Exoplanet Science Institute, 770 South Wilson Avenue, Pasadena, CA 91106, USA
[33] NASA Goddard Space Flight Center, 8800 Greenbelt Road, Greenbelt, MD 20771, USA
[34] University of Maryland, Baltimore County, 1000 Hilltop Circle, Baltimore, MD 21250, USA
[35] Department of Physics and Astronomy, University of New Mexico, 210 Yale Boulevard NE, Albuquerque, NM 87106, USA
[36] Department of Earth, Atmospheric and Planetary Sciences, Massachusetts Institute of Technology, Cambridge, MA 02139, USA
[37] Department of Aeronautics and Astronautics, MIT, 77 Massachusetts Avenue, Cambridge, MA 02139, USA
[38] Department of Astrophysical Sciences, Princeton University, Princeton, NJ 08544, USA
Received 2022 September 30; revised 2023 January 17; accepted 2023 February 6; published 2023 March 28

Abstract

The K-type star TOI-2525 has an estimated mass of $M = 0.849^{+0.024}_{-0.033}\ M_{\odot}$ and radius of $R = 0.785^{+0.007}_{-0.007}\ R_{\odot}$ observed by the TESS mission in 22 sectors (within sectors 1 and 39). The TESS light curves yield significant transit events of two companions, which show strong transit timing variations (TTVs) with a semiamplitude of ∼6

* Based on observations collected at the European Organization for Astronomical Research in the Southern Hemisphere under MPG program 0104.A-9007. This paper includes data gathered with the 6.5 m Magellan Telescopes located at Las Campanas Observatory, Chile.
[39] ESA Research Fellow.

hr. We performed TTV dynamical and photodynamical light-curve analysis of the TESS data combined with radial velocity measurements from FEROS and PFS, and we confirmed the planetary nature of these companions. The TOI-2525 system consists of a transiting pair of planets comparable to Neptune and Jupiter with estimated dynamical masses of $m_{\rm b} = 0.088^{+0.005}_{-0.004}$ and $m_{\rm c} = 0.709^{+0.034}_{-0.033}$ $M_{\rm Jup}$, radii of $r_b = 0.88^{+0.02}_{-0.02}$ and $r_c = 0.98^{+0.02}_{-0.02}$ $R_{\rm Jup}$, and orbital periods of $P_{\rm b} = 23.288^{+0.001}_{-0.002}$ and $P_{\rm c} = 49.260^{+0.001}_{-0.001}$ days for the inner and outer planet, respectively. The period ratio is close to the 2:1 period commensurability, but the dynamical simulations of the system suggest that it is outside the mean-motion resonance (MMR) dynamical configuration. Object TOI-2525 b is among the lowest-density Neptune-mass planets known to date, with an estimated median density of $\rho_{\rm b} = 0.174^{+0.016}_{-0.015}$ g cm^{-3}. The TOI-2525 system is very similar to the other K dwarf systems discovered by TESS, TOI-2202 and TOI-216, which are composed of almost identical K dwarf primaries and two warm giant planets near the 2:1 MMR.

Unified Astronomy Thesaurus concepts: Exoplanet astronomy (486); Exoplanets (498); Exoplanet systems (484)

1. Introduction

As of 2022 September, exoplanet surveys had discovered over 5000 confirmed planets, many of which reside in multiple-planet systems. The current population of multiple-planet systems is a fingerprint of the planet formation and migration mechanisms. Many scholars are confident that planet migration must have occurred simultaneously for all planets in the system, but despite the large efforts to understand the interactions between planets and the protoplanetary disk (Goldreich & Tremaine 1979; Lin & Papaloizou 1979; Ida & Lin 2010; Kley & Nelson 2012; Baruteau et al. 2014; Coleman & Nelson 2014; Levison et al. 2015; Kanagawa et al. 2018; Bitsch et al. 2020; Matsumura et al. 2021; Schlecker et al. 2021a), the planet migration rate, direction, and eccentricity excitation or damping as a function of disk viscosity, mass, and metallicity are still the subject of ongoing research. Warm massive planet pairs near the low-order 2:1 commensurability are rare but have the potential to reveal important details of the disk–planet interactions during the system formation stage.

The current planet formation theories suggest that Jovian planets must have formed further out beyond the so-called ice line and migrated inward toward warm orbits before the primordial disk dissipated. These objects are not easily understood within standard formation models that require rapid accretion of gas by a solid embryo before the stellar radiation dissipates the gas from the protoplanetary disk. This rapid, solid accretion is favored beyond the snow line. Giant planets are then expected to migrate from a couple of astronomical units to the inner regions of the system to produce the population of hot ($P < 10$ days) and warm (10 days $< P <$ 300 days) Jovian or Neptune-mass planets. Typical migration mechanisms can be divided into two groups: disk migration (e.g., Lin & Papaloizou 1986) and high-eccentricity tidal migration (e.g., Rasio & Ford 1996; Fabrycky & Tremaine 2007; Bitsch et al. 2020). These two mechanisms predict significantly different orbital configurations for the migrating planet, and the characterization of these properties, particularly for warm Jovian planets (Huang et al. 2016; Petrovich & Tremaine 2016; Santerne et al. 2016; Dong et al. 2021), can be used to constrain migration theories.

In this context, it is fundamentally important to measure the dynamical mass and orbital eccentricity of the warm Jovian planets. For many systems, this can only be achieved by combining precise transit and radial velocity (RV) observational data. NASA's Transiting Exoplanet Survey Satellite (TESS; Ricker et al. 2015) aims to detect planets through the transit method around relatively bright stars that are suitable for precise Doppler follow-up in order to determine the planetary mass, radius, and bulk density, among other important physical parameters. TESS has already led to more than 230 newly discovered planets, most of which were confirmed by Doppler spectroscopy (e.g., Dumusque et al. 2019; Kossakowski et al. 2019; Luque et al. 2019; Trifonov et al. 2019; Wang et al. 2019; Espinoza et al. 2020; Schlecker et al. 2020; Teske et al. 2020, among many).

In this paper, we report the discovery of another warm massive planet pair around a K dwarf star that has been uncovered by TESS. This work is part of our Doppler data survey and orbital analysis efforts performed within the Warm gIaNts with tEss (WINE) collaboration, which focuses on the systematic characterization of TESS transiting warm giant planets (e.g., Brahm et al. 2019, 2020; Jordán et al. 2020; Schlecker et al. 2020; Trifonov et al. 2021). We present TOI-2525 (TIC 149601126[40]), a two-planet system that exhibits strong transit timing variations (TTVs) of the two transiting signals detected in TESS multisector and ground-based photometry data. This strong TTV signal in the TOI-2525 system points to strongly interacting warm giant–mass planets close to the 2:1 mean-motion resonance (MMR) commensurability.

In Section 2, we present the observational data used to detect and characterize the warm pair of planets orbiting TOI-2525. In Section 3, we introduce the stellar parameter estimates of TOI-2525. In Section 4, we present the results of our orbital analysis, which was performed on the extracted TTVs of the planetary signals, and a self-consistent photodynamical modeling scheme performed jointly with the acquired Doppler data. In Section 4, we also provide results from an analysis of the dynamical architecture and long-term stability of the TOI-2525 system. In Section 5, we discuss the system's architecture and possible formation and evolution and the interior of the planets. Finally, in Section 6, we present a brief summary and our conclusions.

2. Data

Here we present the photometric light-curve and Doppler data acquired for TOI-2525. The TESS space-based photometry is used for transit event identification of TOI-2525 b and c, whereas additional ground-based photometry was used for further TTV analysis and planetary radius estimates. Precise Doppler data were collected for further constraining the planetary masses and eccentricities but also for the stellar parameter estimates of TOI-2525.

[40] Similar to TOI-2202, aka TIC 358107516 (Trifonov et al. 2021), TOI-2525 was known to us as TIC 149601126. The target became a TESS Object of Interest (TOI; Guerrero et al. 2021) while this work was in preparation. Consequently, we adopted the TOI-2525 designation for consistency with the TESS survey.

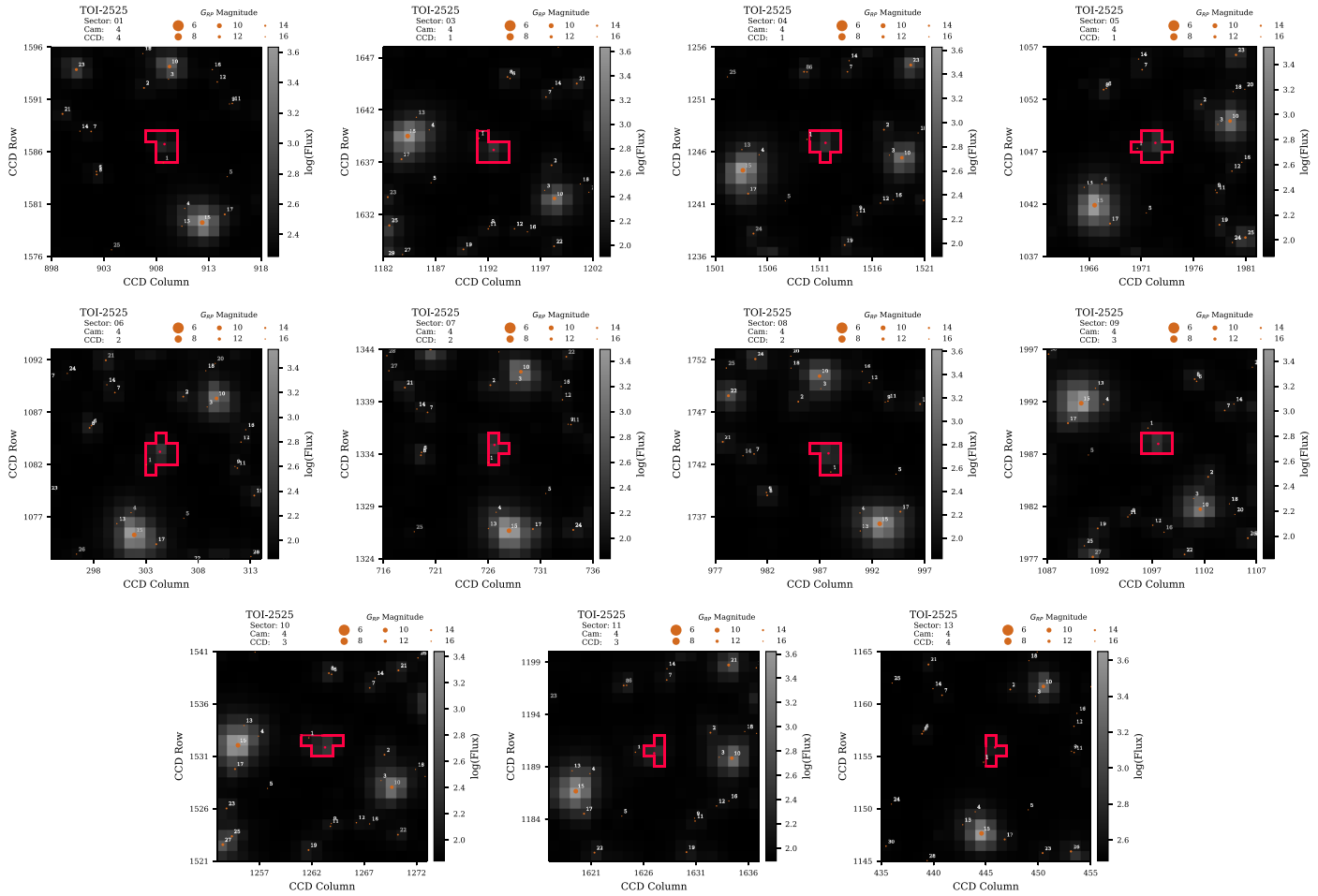

Figure 1. Target pixel file image of TOI-2525 in the FFIs of TESS sectors 1, 3–11, and 13. The central (red) borders in the pixel space are the ones used to construct the TESSERACT photometry. Gaia targets are marked with red circles, whose size has been coded by their *G* magnitude.

2.1. TESS

Object TOI-2525 was observed in sectors 1, 3–11, and 13 during the first year of the TESS primary mission with a 30 minute cadence and sectors 27, 28, and 30–39 with a 2 minute cadence in the third mission year. Objects TOI-2525 b and c were identified in the light curves extracted from the TESS full-frame images (FFIs) using the TESSERACT[41] pipeline (F. Rojas et al. 2023, in preparation). A brief introduction of our FFI extraction with TESSERACT in the context of the WINE collaboration can be found in Schlecker et al. (2020), Gill et al. (2020), and Trifonov et al. (2021). Figure 1 shows the target pixel file image of TOI-2525 constructed from the TESS FFI image frames and Gaia DR3 data (Gaia Collaboration et al. 2021). Figure 1 shows that there are no bright contaminators in the FFI aperture (red solid contour); thus, we concluded that the transit signals are indeed coming from TOI-2525 and not from neighboring stars. This was later confirmed by ground-based transit detections of TOI-2525 b and c. However, a fainter source labeled "1" is occasionally in the FFI aperture, which dilutes the FFI light curves. Since TESSERACT does not correct contamination in the TESS apertures from nearby stars, we follow the same methodology as used in Trifonov et al. (2021) to calculate and apply a dilution correction for the contamination of TOI-2525 on the FFI light curves.

We retrieved the 2 minute cadence light curves from the Mikulski Archive for Space Telescopes.[42] The Science Processing Operations Center (Jenkins et al. 2016) provides simple aperture photometry (SAP) and systematics-corrected presearch data conditioning (PDC) photometry (Smith et al. 2012; Stumpe et al. 2012). The PDCSAP light curves are corrected for contamination from nearby stars and instrumental systematics originating from, e.g., pointing drifts, focus changes, and thermal transients. In our work on TOI-2525, for the 2 minute cadence data, we only use the corrected PDCSAP data.

2.2. ASTEP

The Antarctica Search for Transiting ExoPlanets (ASTEP; Guillot et al. 2015) instrument is a 40 cm Newton telescope installed in 2010 at the Concordia station, located at −75.06°S, 123.3°E and an altitude of ∼3230 m. ASTEP is a robotic telescope dedicated to photometric observations of the fields of stars and their exoplanets.

Due to the extremely low data transmission rate at the Concordia station, the data are processed automatically on site using an IDL-based aperture photometry pipeline (Mékarnia et al. 2016). The raw light curves of up to 1000 stars of the field are transferred to Europe on a server in Roma, Italy, and then

[41] https://github.com/astrofelipe/tesseract

[42] https://mast.stsci.edu/portal/Mashup/Clients/Mast/Portal.html

available for deeper analysis. These data files contain each star's flux computed through 10 fixed circular aperture radii, so that optimal calibrated light curves can be extracted.

Thanks to the accurate TTV model prediction constructed on the TESS data, we scheduled successful observations with ASTEP of TOI-2525 b and c. For TOI-2525 b, we detected a full and a partial transit event on the nights of UT 2021-09-17 and UT 2022-06-23, respectively, whereas for TOI-2525c, we observed two full transit events on the nights of UT 2021-04-15 and UT 2022-07-02 and two partial transit events on the nights of UT 2021-06-3 and UT 2021-09-10.

2.3. Observatoire Moana

A partial transit of TOI-2525c was observed with the Siding Spring Observatory station of the Observatoire Moana telescope network (OM-SSO). The OM-SSO is an RC Optical Systems RCOS20 f8.1 telescope with a focal length of 3980 mm. It is equipped with an FLI Microline 16803 camera with 4k × 4k pixels of 9 with a pixel scale of 0.″47 and a field of view of 30′ × 30′. Observations were taken using an Astrodon Exoplanet (clear blue blocking) filter. Observations of TOI-2525c were performed on 2021 October 29 covering an ingress. The adopted exposure time was 147 s, and the airmass ranged from 1.15 to 2. The OM-SSO data were processed with a dedicated automated pipeline adapted from a version that was initially developed for obtaining differential photometry of Las Cumbres Observatory Global Telescope (LCOGT) light curves (Espinoza et al. 2019).

2.4. LCOGT

We observed one partial transit of TOI-2525b and two partial transits of TOI-2525c using the LCOGT 1.0 m network (Brown et al. 2013) nodes at the Cerro Tololo Inter-American Observatory (CTIO) and South Africa Astronomical Observatory (SAAO). The 1 m telescopes are equipped with 4096 × 4096 SINISTRO cameras having a pixel scale of 0.″389 pixel^{-1}, resulting in a field of view of 26′ × 26′. The TOI-2525b transit was observed from SAAO on 2022 January 11 in the Sloan g' and i' filters using a 4.″3 target aperture. Transits of TOI-2525c were observed twice from CTIO on 2021 December 18 and 2022 February 5 in the Sloan g' and i' filters, respectively, using 4.″0–4.″7 target apertures. The LCOGT data reduction and photometric measurements were performed using the AstroImageJ (Collins et al. 2017) software package.

2.5. Planet Finder Spectrograph

Object TOI-2525 was monitored with the Planet Finder Spectrograph (PFS; Crane et al. 2006, 2008, 2010) installed at the 6.5 m Magellan/Clay telescope at Las Campanas Observatory. It was observed with the iodine gas absorption cell of the instrument at four different observing runs between 2020 November 3 and 2021 November 16, adopting an exposure time of 1200 s and using a 3 × 3 CCD binning mode to minimize read noise. Object TOI-2525 was also observed without the iodine cell in order to generate the template for computing the RVs, which were derived following the methodology of Butler et al. (1996). The mean uncertainty of the PFS RVs of TOI-2525 is 5.7 m s^{-1}. The PFS RVs are presented in Table 1.

Table 1
FEROS and PFS RV Measurements of TOI-2525

BJD	RV (m s^{-1})	RV$_\sigma$ (m s^{-1})	Instrument
2,458,904.623	−48,154.684	18.000	FEROS
2,458,923.562	−48,184.684	18.100	FEROS
2,459,156.792	320.393	4.235	PFS
2,459,157.754	310.269	6.285	PFS
2,459,238.635	225.396	6.960	PFS
2,459,239.607	255.721	6.470	PFS
2,459,501.824	337.951	5.040	PFS
2,459,504.843	345.583	5.150	PFS
2,459,505.837	341.083	5.400	PFS
2,459,531.781	295.292	7.340	PFS
2,459,534.809	320.755	5.480	PFS

2.5.1. FEROS

We obtained three Doppler measurements of TOI-2525 with the FEROS spectrograph (Kaufer et al. 1999) installed at the MPG 2.2 m telescope at La Silla Observatory. These spectra were taken on BJD = 2,458,904.623, 2,458,914.612, and 2,458,923.562 with the simultaneous ThAr wavelength calibration technique. The exposure times were set to 1800 s, yielding an average signal-to-noise ratio of 25. The FEROS data were reduced, extracted, and analyzed with the `ceres` pipeline (Brahm et al. 2017a) delivering RV and bisector span measurements with a mean uncertainty of 19 m s^{-1}. The RV datum obtained on BJD = 2,458,914.612, however, was a clear outlier with poor accuracy due to bad weather conditions. Therefore, we could rely on only two FEROS spectra, which are fully consistent with the orbital fit to the TTVs and the PFS data. However, the two FEROS RVs have no effective weight on the orbital fit, since their contribution is canceled by the two additional fitting parameters RV$_{\rm off.\ FEROS}$ and RV$_{\rm jit.\ FEROS}$. Thus, we decided to not use the FEROS RVs in our orbital analysis. The obtained FEROS RVs are presented in Table 1.

3. Stellar Parameters of TOI-2525

Visible in the southern hemisphere, TOI-2525 is an early K-type star. The star has a distance of 400.0 ± 2.3 pc from the Sun and an apparent magnitude of 13.4 mag in the TESS bandpass. The atmospheric and physical parameters were obtained using three coadded FEROS spectra and the `ZASPE` code (Brahm et al. 2017b). This code compares the stellar spectra with synthetic atmospheric models generated from the ATLAS9 model atmospheres (Castelli & Kurucz 2004). The result is generated using the χ^2 method at regions in the spectra that are most sensitive to changes. Parameters obtained from these regions are calculated iteratively. The errors of the values are generated with Monte Carlo simulations for the depth of the spectral lines. For TOI-2525, an effective temperature of $T_{\rm eff} = 5096 \pm 80$ K, a metallicity of [Fe/H] = 0.14 ± 0.05 dex with respect to the solar metallicity, and a projected rotational velocity of $v \sin i = 1.5 \pm 0.3$ km s^{-1} were calculated.

The physical parameters are estimated as in Brahm et al. (2020). We used the PARSEC stellar isochrones (Bressan et al. 2012), which contain the absolute magnitudes of several bandpasses for a set of ages, masses, and metallicities. Since the latter were already calculated in the first step, they are fixed in the subsequent iteration. Using the spectroscopic temperatures, Gaia parallaxes, and observed magnitudes, the age and mass were obtained via a Markov Chain Monte Carlo (MCMC)

Table 2
Stellar Parameters of TOI-2525 and Their 1σ Uncertainties Derived Using ZASPE Spectral Analyses, Gaia Parallax, Broadband Photometry, and PARSEC Models

Parameter	TOI-2525	Reference
Spectral type	K8V	(1)
Distance (pc)	$400^{+2.3}_{-2.3}$	(2)
Mass ($M_\odot$)	$0.849^{+0.024}_{-0.033}$ (0.042)	This paper
Radius ($R_\odot$)	$0.785^{+0.007}_{-0.007}$ (0.031)	This paper
Luminosity ($L_\odot$)	$0.363^{+0.016}_{-0.016}$ (0.008)	This paper
Age (Gyr)	$3.99^{+4.30}_{-2.60}$	This paper
A_V (mag)	$0.287^{+0.070}_{-0.074}$	This paper
$T_{\rm eff}$ (K)	5096 ± 80 (102)	This paper
$\log g$ [cm · s^{-2}]	4.58 ± 0.20	This paper
[Fe/H]	0.14 ± 0.05	This paper
$v \cdot \sin(i)$ (km s^{-1})	1.5 ± 0.3	This paper

Note. (1) ESA (1997), (2) Gaia Collaboration (2018), Gaia Collaboration et al. (2016). The values in parentheses are "floor" (i.e., more realistic, minimum) uncertainties predicted by Tayar et al. (2022) and adopted in our work.

exploration of the parameter space using the `emcee` package (Foreman-Mackey et al. 2013). The result is an age of $3.99^{+4.3}_{-2.6}$ Gyr, a mass of $M_\star = 0.849^{+0.024}_{-0.033}\,M_\odot$, and a radius of $R_\star = 0.785 \pm 0.007\,R_\odot$. Our relatively small uncertainties in the `ZASPE` stellar parameters, however, are internal and do not include possible systematic differences with respect to other stellar models. Therefore, we followed the prescription of Tayar et al. (2022), who suggested a systematic uncertainty floor of order ∼5% in mass, ∼4% in radius, and ∼2% in temperature and luminosity (see Tayar et al. 2022, for more details). We adopt these relative uncertainties to access more realistic stellar parameter errors throughout this work. The full set of atmospheric and physical parameters is given in Table 2.

4. Analysis and Results

4.1. Preliminary Data Vetting

We identify the transit events of TOI-2525 b and c in the first-year TESS FFI light curves. Our preliminary transit characterization methodology includes detrending of the TESSERACT FFI light curves with a robust (iterative) Matérn Gaussian process (GP) kernel via the WOTAN package (see Hippke et al. 2019) and a transit signal search with the `transitleastsquares` (TLS; Hippke & Heller 2019) algorithm.

Figure 2 shows our TLS results on the combined TESS FFI light-curve data of TOI-2525. We first detect the stronger transit signal of TOI-2525c with a period of ≈49.3 days. We filter this signal by applying a Keplerian transit model with the obtained parameters from the TLS, and we seek additional transit signals in the model residuals. We clearly find the shallower but more frequent transit signal of the inner planet TOI-2525b at a period of $P_b = 23.3$ days. Figure 2 shows many other significant TLS peaks with a signal detection efficiency (see Hippke & Heller 2019) of >8.3 that are nothing more than the integer subharmonics of the transit signals.

From the FFI data, we found that the light-curve mid-transit time of TOI-2525b and TOI-2525c are not linear in time and show strong deviations in the expected times of transit, i.e., TTVs.

The available Doppler data of TOI-2525 are too few for an independent RV validation of the two-planet system (see Table 1). Since we identified the transit events in 2019, we have made many attempts to collect precise spectroscopic data from the southern hemisphere. However, TOI-2525 is faint and requires significant observational efforts and excellent sky conditions. This, in combination with the COVID-19 pandemic closures of the ESO and Las Campanas observatories, prevented us from obtaining sufficient RV data. Nonetheless, we conclude that at this point, the PFS data alone are adequate for validation of the system when combined with the transit periods from TESS and can contribute to the planetary mass estimates when combined with the strong TTVs.

4.1.1. Extraction of TTVs

The TTVs were estimated by fitting all of the available photometric data using the EXOPLANET software package (Foreman-Mackey et al. 2021). We used the descriptive model TTVORBIT, which assumes Keplerian orbits for each planet but allows for the central time of each transit to be a free parameter in the model. The parameters of the model are the values of R_p for each planet, their impact parameters b, the transit times, the stellar mass $M_\star$ and density $\rho_\star$, quadratic limb-darkening coefficients u_1 and u_2 for each instrument used, and parameters to describe trends and correlations in the data. Regarding the latter, we adopt a linear model in time for the ground-based transits, which are often only partially observed, and a GP for each of the short- and long-cadence TESS data sets. The GP kernel adopted is a damped simple harmonic oscillator (Foreman-Mackey et al. 2017a) with $Q = 1/3$, variance $\sigma_{\rm GP}$, and correlation length parameter $\rho_{\rm GP}$.

Table 3 lists the resulting light-curve parameters, whereas Figure 3 shows the resulting light-curve models applied to all photometric data sets. Both TOI-2525 transit signals exhibit strong TTV libration. The values of the fitted transit times for each transit are listed in Table A2.

4.2. Orbital Analysis

4.2.1. Joint RV and TTV Analysis

For the joint RV and TTV orbital analysis of the TOI-2525 system, we followed a similar route to the one we used in Trifonov et al. (2021) for the modeling of the TOI-2022 system. We refer the reader to that paper for a more detailed description of the chosen methodology. Briefly, for TOI-2525, we performed orbital fitting with the EXO-STRIKER exoplanet toolbox[43] (Trifonov 2019) by adopting the self-consistent dynamical model on the extracted TTVs from Section 4.1.1. The TTV model can provide a relatively inexpensive orbital and dynamical solution to the system in terms of CPU time. However, it also comes with a severe ambiguity in eccentricity versus dynamical planetary mass (e.g., Lithwick et al. 2012; Dawson et al. 2021; Trifonov et al. 2021). Therefore, we fit the TTVs jointly with the RV data from PFS to better constrain the planetary dynamical masses and eccentricities. The RV model is intrinsic to EXO-STRIKER, whereas the TTV model is wrapped around the TTVFAST package (Deck et al. 2014). The fitted parameters for each planet were the RV semiamplitude K (which is automatically converted to the dynamical planetary mass m_p), orbital period P, eccentricity e, argument of periastron ω, and mean anomaly M_0. Our TTV+RV modeling scheme allows a difference in the planetary inclinations

[43] https://github.com/3fon3fonov/exostriker

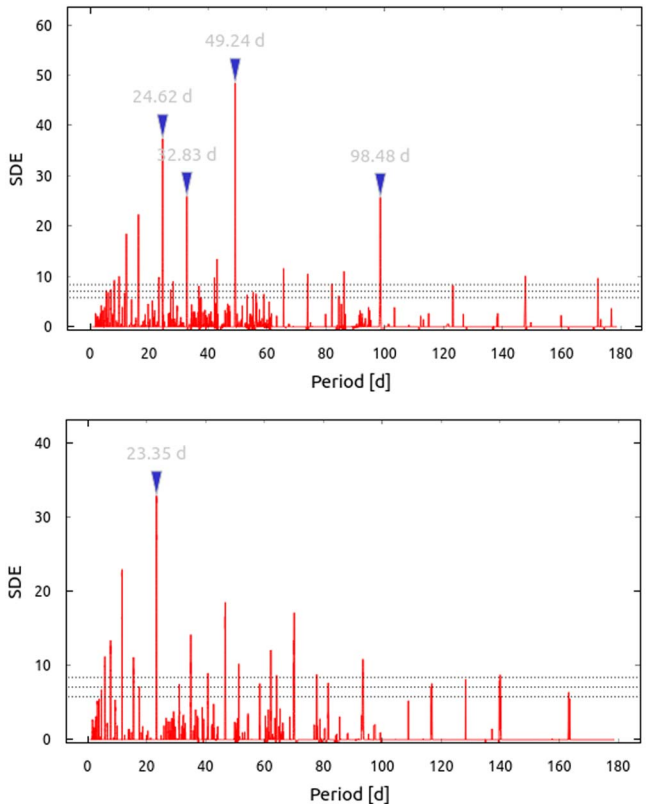

Figure 2. The top panel shows the TLS power spectra of the detrended TESS FFI light-curve data of TOI-2525. The planetary transit signal of the more massive planet c is detected at $P_c = 49.24$ days. The bottom panel shows the TLS power spectra of the residuals, which reveal the transit signal of the inner, less massive planet at $P_b = 23.3$ days. The remaining TLS peaks are harmonics and subharmonics of the transit signals. Horizontal dashed lines indicate signal detection efficiency (Hippke et al. 2019) power levels of 5.7, 7.0, and 8.3, which correspond to TLS false-positive rates of 10%, 1%, and 0.1%.

Table 3
Planetary Radii, Orbital Inclinations, and Stellar Density and Mass Estimates of the TOI-2525 System Derived during TTV Extraction

Parameter	Median	σ
r_b ($R_{\rm Jup}$)	0.88	0.02
r_c ($R_{\rm Jup}$)	0.98	0.02
i_b (deg)	89.31	0.03
i_c (deg)	89.96	0.03
$\rho_\star$ (g cm^{-3})	2.14	0.04
$M_\star$ ($M_\odot$)	0.85	0.05

Note. The remaining transit light-curve data parameter estimates are listed in Table A1, whereas the individual transit times for TOI-2525 b and c are listed in Table A2.

($\Delta i \geqslant 0°$). Thus, we also model the orbital inclinations i and the difference between the line of node $\Delta\Omega$. All of these parameters are valid for BJD = 2,458,333.52, which is an arbitrary epoch chosen slightly before the first transit event of the inner planet. The RV data offset and jitter[44] parameters of PFS added two more free parameters.

Finally, our dynamical model, particularly the planetary masses, also depends on the stellar mass estimate of TOI-2525, for which we adopt a fixed value of 0.849 $M_\odot$. We set the time step in the dynamical model to $dt = 0.02$ days to assure sufficient orbital resolution and accuracy.

We ran a nested sampling (NS) scheme (Skilling 2004), which allowed us to efficiently explore the complex parameter space of osculating orbital elements and study the parameter posteriors and overall dynamics. Our NS run was performed with the DYNESTY sampler (Speagle 2020), which is integrated into EXO-STRIKER. We ran 100 "live points" per fitted parameter using the "Dynamic" NS scheme, focused on 100% posterior convergence instead of log evidence (see Speagle 2020 for details). Parameter priors were estimated by running several experimental NS runs and adopting a wide range of uniform parameter priors. After a few consecutive NS runs, we narrowed the adequate parameter space to be explored. We note that we adopted very narrow priors on the orbital inclinations to ensure that the TTV+RV model parameter space is consistent with the inclination estimates extracted from the TTVs. Thus, we eliminate configurations that could explain the RV data but would not lead to transit events (i.e., impact parameters $b_{\rm b}$ and $b_{\rm c}$, which are inconsistent with the light-curve signal). The final adopted parameter priors are listed in Table 4.

Figures 4 and 5 show the TTV and RV data together with the best-fit joint dynamical model of TOI-2525. The left and right panels of Figure 4 show the TTVs of TOI-2525b and c, respectively, fitted with the best-fit TTV model. Figure 5 shows the RV component of the best-fit model applied to the PFS RVs. Figure 5 also shows the two FEROS RVs fitted independently to the best fit with an optimized offset. The middle and right panels of Figure 5 show a phase-folded representation of the RV signals of TOI-2525b and c, respectively, modeled with an osculating period. The signal of the inner planet TOI-2525b is strongly overshadowed by the dominating signal of the outer one due to the large difference in K amplitudes (see Table 4).

The final posterior probability distributions with an RV linear trend are shown in Figure A1. Our final estimates for TOI-2525b and c lead to planetary orbital periods of $P_b = 23.288^{+0.001}_{-0.002}$ and $P_c = 49.260^{+0.001}_{-0.001}$ days, eccentricities of $e_b = 0.159^{+0.012}_{-0.007}$ and $e_c = 0.152^{+0.006}_{-0.005}$, and dynamical masses of $m_b = 0.088^{+0.005}_{-0.004}$ and $m_c = 0.709^{+0.034}_{-0.034}$ $M_{\rm Jup}$. The mutual inclination is constrained to $\Delta i = 2.^{\circ}0^{+1.9}_{-1.2}$. Given the planetary radii obtained during the TTV extraction in Section 4.1.1, we derive a remarkably low density of $\rho_b = 0.174^{+0.016}_{-0.015}$ g cm^{-3} for the inner planet and $\rho_c = 1.014^{+0.084}_{-0.076}$ g cm^{-3} for the outer one. The full list of posterior and maximum $-\ln \mathcal{L}$ (i.e., best-fit) estimates was derived from the joint TTV+RV model and listed in Table 4.

4.2.2. Joint RV and Photodynamical Analysis

A complementary analysis of the light curves and RVs of TOI-2525 was performed using the `flexifit` [45] python package. For modeling the photometric data, `flexifit` employs analytic transit light curves (Mandel & Agol 2002) with quadratic limb darkening. Dynamical effects are included via the `rebound` N-body package (Rein & Liu 2012). Our

[44] That is, the unknown excess variance of the data, which we add in quadrature to the RV error budget while we evaluate the model's $-\ln \mathcal{L}$ (Baluev 2009) and substantially build the NS posteriors.

[45] https://gitlab.gwdg.de/sdreizl/exoplanet-flexi-fit

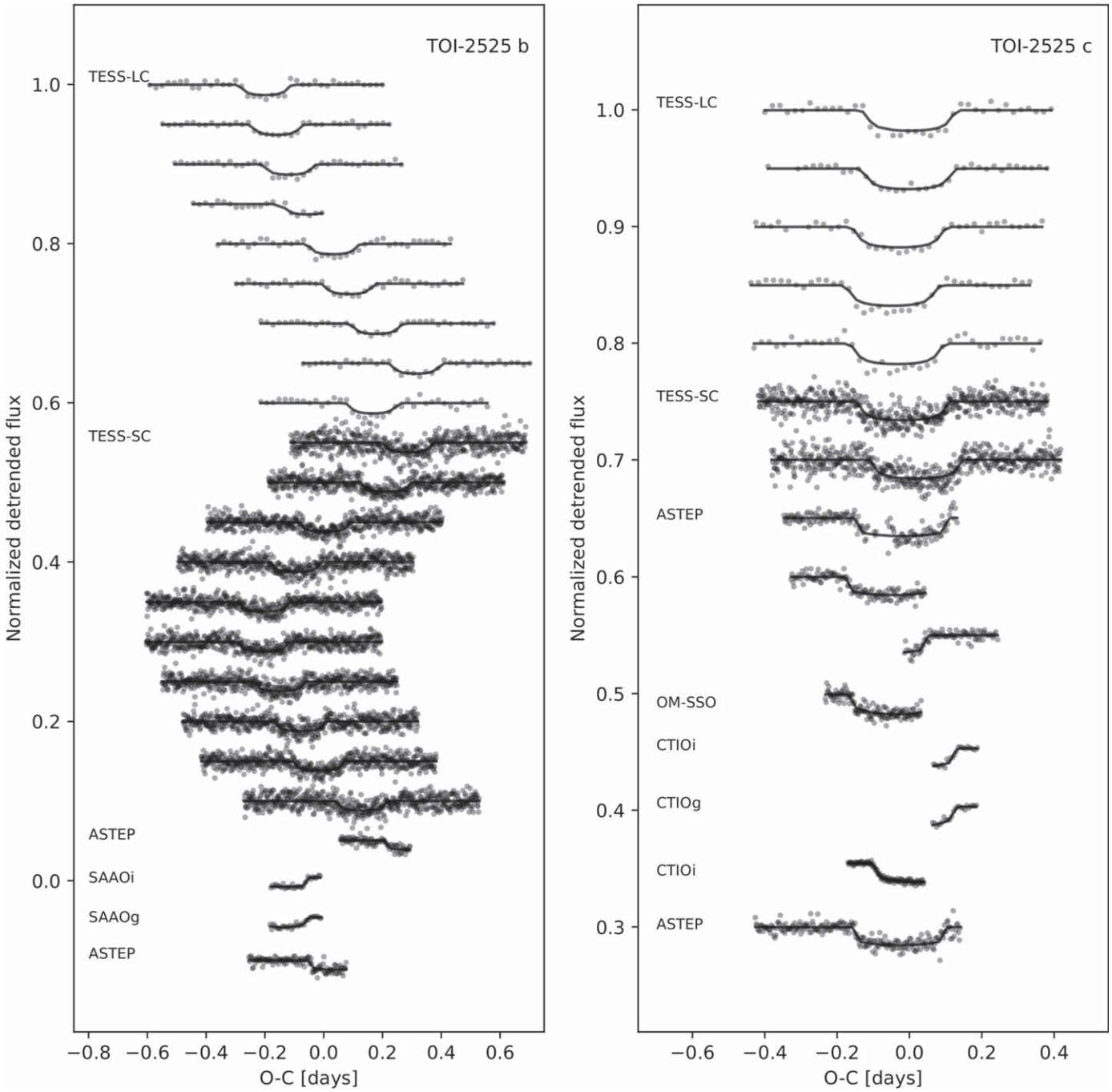

Figure 3. TESS light-curve data and model of the TOI-2525 transit signals, plotted with arbitrary vertical offsets. The left panel shows the transit signal of the inner planet TOI-2525 b and its strong TTV variation, whereas the right panel shows the same for the outer, more massive Jovian planet TOI-2525c. The *x*-axis of the curves for TOI-2525 b is t_n-1333.5070mod23.2915 days, and for TOI-2525c is t_n-1335.4101mod49.2424 days.

orbital analysis with `flexifit` is performed in Jacobi coordinates using the `ias15` integrator (Everhart 1985), which automatically determines the numerical time step *dt* down to machine precision. The fitting with `flexifit` relies on an MCMC parameter sampling provided by the `emcee` sampler (Foreman-Mackey et al. 2013), which converges to the posterior probability distribution.

The `flexifit` model provides orbital parameters valid for the epoch BJD = 2,458,333.52, which is the same as the one chosen for joint TTV+RV analysis (see Section 4.1.1). We chose uniform parameter priors that define an equal probability of occurrence between predefined borders. Most of the priors were generously defined, covering a large section of parameter space. The only priors worth mentioning are for the periods $P_b \in \mathcal{U}(23.1,23.4)$, $P_c \in \mathcal{U}(49.1,49.4)$ days, which are sufficient considering the mid-transit times, and the inclinations $i_b \in \mathcal{U}(81,99)$, $i_c \in \mathcal{U}(81,99)$ degrees, which can be restricted to these intervals for geometrical reasons, because we do observe transits. The remaining priors of the photodynamical model are listed in Table A3. With the stellar parameters (Table 2) and quadratic limb-darkening coefficients given, our free orbital parameters for each planet are the orbital period *P*, mass *m*, eccentricity *e*, longitude of periastron ω, time of first conjunction with respect to the start of integration t_{conj},

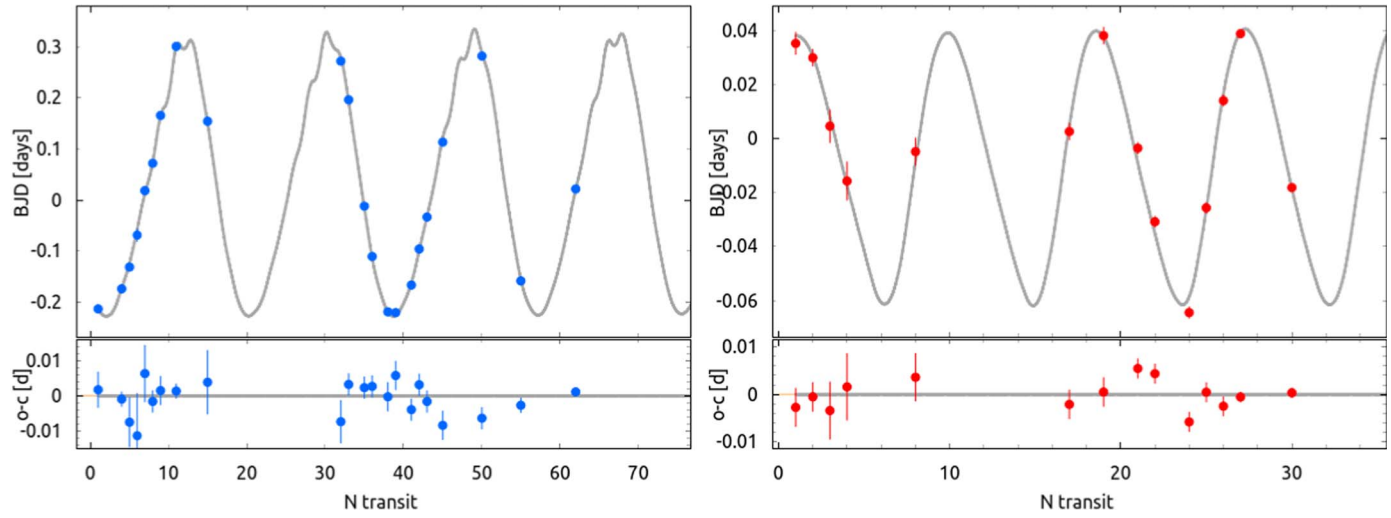

Figure 4. The TTVs of TOI-2525 b (blue) and TOI-2525 c (red), fitted with a two-planet dynamical model jointly with the RVs from PFS. The top panels show the TTV time series and best-fit model for each planet, whereas the bottom panels show the TTV residuals.

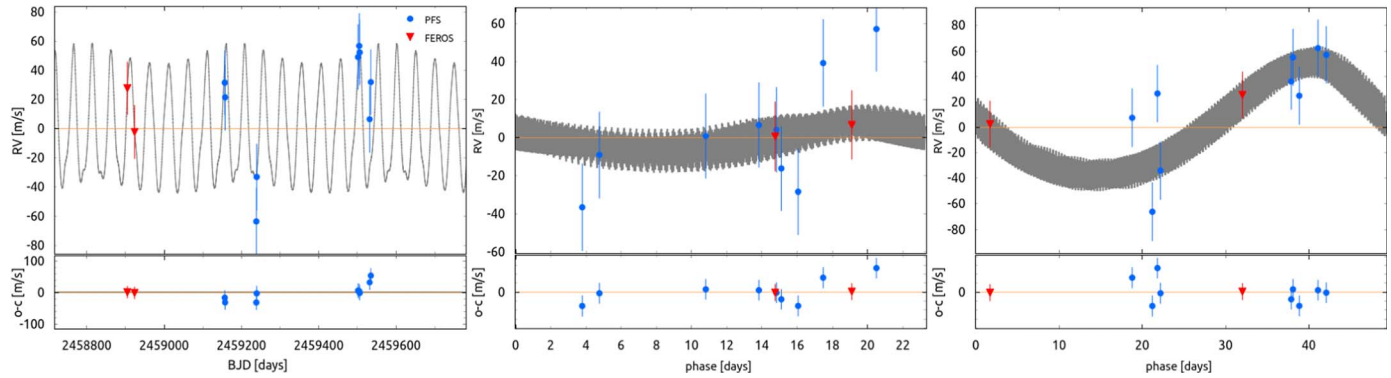

Figure 5. The RV component of the two-planet dynamical model of TOI-2525, constructed jointly with the TTV data and the RVs from PFS (blue circles). The two RVs from FEROS (red triangles) are overplotted with an optimized RV offset to the model. The left panel shows the time series and the *N*-body model, and the middle and right panels show a phase-folded representation of the RV data modeled with the dynamical model (with an osculating period). The PFS data uncertainties include the estimated RV jitter added in quadrature to the error budget, while the FEROS data are plotted with their nominal RV uncertainties. The small subpanels show the RV residuals.

Table 4
NS Priors, Posteriors, and the Optimum $-\ln \mathcal{L}$ Orbital Parameters of the Two-planet System TOI-2525 Derived by Joint Dynamical Modeling of TTVs (TESS, ASTEP, SSO, and LCOGT) and RVs (FEROS and PFS)

	Median and 1σ		Max. $-\ln \mathcal{L}$		Adopted Priors	
Parameter	Planet b	Planet c	Planet b	Planet c	Planet b	Planet c
K (m s^{-1})	$7.1^{+0.3}_{-0.3}$	$44.4^{+1.5}_{-1.5}$	7.1	44.4	$\mathcal{U}$(5.0,30.00)	$\mathcal{U}$(20.0,60.0)
P (days)	$23.288^{+0.001}_{-0.002}$	$49.260^{+0.001}_{-0.001}$	23.289	49.260	$\mathcal{U}$(23.2,23.4)	$\mathcal{U}$(49.1,49.4)
e	$0.159^{+0.012}_{-0.007}$	$0.152^{+0.006}_{-0.005}$	0.171	0.160	$\mathcal{U}$(0.0,0.4)	$\mathcal{U}$(0.0,0.4)
ω (deg)	$346.3^{+0.7}_{-0.7}$	$21.8^{+0.8}_{-0.8}$	346.5	22.0	$\mathcal{U}$(0.0,360.0)	$\mathcal{U}$(0.0,360.0)
M_0 (deg)	$120.8^{+0.6}_{-0.5}$	$71.2^{+1.2}_{-1.0}$	120.6	71.6	$\mathcal{U}$(0.0,360.00)	$\mathcal{U}$(0.0,360.00)
λ (deg)	$107.0^{+0.8}_{-0.8}$	$93.4^{+0.9}_{-1.0}$	107.1	93.1	(derived)	(derived)
i (deg)	$89.96^{+0.08}_{-0.07}$	$89.99^{+0.08}_{-0.06}$	89.97	89.99	$\mathcal{N}$(90.0,0.1)	$\mathcal{N}$(90.0,0.1)
Ω (deg)	0.0	$2.0^{+1.9}_{-1.2}$	0.0	1.9	(fixed)	$\mathcal{N}$(0.0,15.0)
Δi (deg)	$2.0^{+1.9}_{-1.2}$	...	1.9	...	(derived)	...
a (au)	$0.1511^{+0.0025}_{-0.0025}$	$0.2491^{+0.0041}_{-0.0042}$	0.1511	0.2491	(derived)	(derived)
m ($M_{\rm Jup}$)	$0.088^{+0.005}_{-0.004}$	$0.709^{+0.034}_{-0.034}$	0.089	0.710	(derived)	(derived)
ρ (g cm^{-3})	$0.174^{+0.016}_{-0.015}$	$1.014^{+0.084}_{-0.076}$	0.174	1.014	(derived)	(derived)
RV$_{\rm off.}$ PFS (m s^{-1})	$-28.5^{+7.1}_{-7.4}$	...	-32.2	...	$\mathcal{U}(-300.00,100.0)$	...
RV$_{\rm jit.}$ PFS (m s^{-1})	$26.8^{+6.8}_{-5.4}$	...	21.5	...	$\mathcal{J}$(0.0,50.0)	...

Note. The orbital elements are in the Jacobi frame and valid for epoch BJD = 2,458,333.52. The adopted priors are listed in the rightmost columns, and their meanings are $\mathcal{U}$, uniform; $\mathcal{N}$, Gaussian; and $\mathcal{J}$, Jeffrey's (log-uniform). The derived planetary posterior parameters of a and m are calculated taking into account the stellar parameter uncertainties (see note in Table 2).

inclination i, and planet-to-star radius ratio R_p/R_s. The longitude of the ascending node Ω was fixed to $\Omega_b = 0$ for the inner planet and free for the outer planet. For the instrumental and observational errors from the RV data from PFS, a jitter parameter and an offset were determined.

The photometric data were separated into eight distinct data sets: TESS FFIs (year 1), TESS PDC (year 3), ASTEP 1-6, CTIO, SSO, and SAAO 1-2. The photometric data from the TESS FFIs in the first TESS year were detrended sector-wise using `rspline` in the `wotan` package (Hippke et al. 2019). For the third year of TESS observations, the 2 minute cadence data from the PDCSAP pipeline, as well as the ground-based photometry data from ASTEP, CTIO, SSO, and SAAO, were included in the model without further detrending. For each data set, an offset was fitted. In total, this adds up to 30 dimensions of fitting; all of the other parameters, including the RV semiamplitude K, are derived.

Figures A2 and A3 show an impression of the light curves for TESS FFI, TESS PDC, ASTEP, and SSO fitted jointly with `flexifit`. The posterior distributions of the MCMC can be seen in Figure A4. Both masses $m_b = 0.084^{+0.005}_{-0.005}$ and $m_c = 0.657^{+0.031}_{-0.032} M_{\rm Jup}$ were estimated to an error of less than 10%. Combined with the planetary radii of $R_b = 0.774^{+0.010}_{-0.010}$ and $R_c = 0.904^{+0.010}_{-0.010} R_{\rm Jup}$, we get a very low density of $\rho_b = 0.226^{+0.015}_{-0.014}$ g cm^{-3} for the inner planet. The density for the outer planet is $\rho_c = 1.11^{+0.07}_{-0.07}$ g cm^{-3}. The planetary densities are slightly larger than our results from the TTV +RV analysis. The orbital parameters, offsets, and jitter parameters from the photodynamical orbital analysis are listed in Table A3.

Here we note that applying a photodynamical model to a system having RV data and large photometric data sets (of the order of 200,000 data points) for more than 1000 days is computationally expensive. On a standard CPU, an iteration of the MCMC takes approximately 2.5 s, which keeps the length of the chain limited. Since the analysis was very time-consuming, it was stopped after 100,000 MCMC iterations. The convergence criterion of 20% mean acceptance fraction was not reached (see Foreman-Mackey et al. 2013), but the physical and dynamical parameters correspond to those from the light curve and RV+TTV analysis presented in Sections 4.1.1 and 4.2.1 and give us confidence in our orbital solution.

4.3. Dynamics and Long-term Stability

Following Trifonov et al. (2021), we inspected the Hill (see Gladman 1993) and angular momentum deficit (AMD; see Laskar & Petit 2017) stability criteria of the TOI-2525 system. In terms of the classical Hill stability criterion, the TOI-2525 planetary system is predicted to be stable. We estimate a mutual Hill distance of $\sim$7.4 $R_{\rm Hill,m}$, which is above the widely accepted distance of $\sim$3.5 $R_{\rm Hill,m}$ for the system to be considered Hill-stable. However, accounting for the estimated orbital eccentricities, semimajor axes, mutual orbital inclinations, and planetary masses of TOI-2525 b and c, the AMD criterion suggests that the TOI-2525 planetary system is unstable. The AMD criterion is very sensitive to eccentricities. Thus, the moderately eccentric orbits of the pair are the reason for the negative AMD result.

As discussed in Trifonov et al. (2021), the AMD and Hill stability criteria are only a proxy for long-term stability and do not account for the system's dynamics near MMRs. Therefore, to test the long-term dynamics and possible MMR in the system, we adopt exactly the same N-body numerical setup used in our recent analysis of TOI-2202 (Trifonov et al. 2021). This is adequate because TOI-2202 and TOI-2525 share somewhat similar physical and orbital characteristics. We refer the reader to Section 5 of Trifonov et al. (2021) for more details about the stability test performed here for TOI-2525. Briefly, we performed numerical integrations using a custom version of the Wisdom–Holman N-body algorithm (Wisdom & Holman 1991), which directly adopts and integrates the Jacobi orbital elements from the posterior orbital analysis. We tested the stability of the TOI-2525 system up to 1 Myr with a small time step of 0.02 days for 10,000 randomly chosen samples from the achieved orbital parameter posteriors from the TTV +RV dynamical modeling scheme. We automatically monitored the evolution of the planetary semimajor axes, eccentricities, secular apsidal angle $\Delta\omega = \omega_{\rm b} - \omega_{\rm c}$, and first-order 2:1 MMR angles $\theta_1 = \lambda_{\rm b} - 2\lambda_{\rm c} + \omega_{\rm b}$ and $\theta_2 = \lambda_{\rm b} - 2\lambda_{\rm c} + \omega_{\rm c}$ (where $\lambda_{\rm b,c} = M_{\rm b,c} + \omega_{\rm b,c}$ is the mean longitude of planets b and c, respectively; see Lee 2004). These angles are important for libration in secular apsidal alignment or MMR.

We found that all 10,000 samples examined are stable for 1 Myr. Figure 6 presents the resulting posterior probability distribution of some of the important dynamical properties of the system, such as mean period ratio $P_{\rm rat}$, mean eccentricities $\hat{e}_{\rm b}$ and $\hat{e}_{\rm c}$, peak-to-peak amplitudes ampl. $e_{\rm b}$ and ampl. $e_{\rm c}$, dynamical masses of the planets $m_{\rm b}$ and $m_{\rm c}$, and orbital semimajor axes $a_{\rm b}$ and $a_{\rm c}$. Figure 6 shows that the period ratio evolution is bimodal, oscillating around either $\sim$2.127 or, more plausibly, $\sim$2.126, which is too far from the exact 2:1 period ratio for the system to librate in the 2:1 MMR. This is confirmed by the circulation of θ_1 and θ_2 (for which distributions are not shown in Figure 6). On the other hand, we observe a bimodality of the evolution of $\Delta\omega$, which is intriguing. About half of the sampled initial conditions lead to libration of $\Delta\omega$ about 0° with a mean semiamplitude around 80°, whereas the rest of the sampled initial conditions seem to exhibit a mean semiamplitude around 180°, i.e., circulation (see Section 5.1 for more explanation of this dynamical behavior).

Figure 7 shows an example of the 1000 yr extent of the orbital evolution simulation started from the best fit (i.e., maximum $-\ln \mathcal{L}$; see Table 4). We show the evolution of the eccentricities, mutual period ratio $P_{\rm rat}$, eccentricities $e_{\rm b}$ and $e_{\rm c}$, and orbital inclinations $i_{\rm b}$ and $i_{\rm c}$. The TOI-2525 system is consistent with moderate eccentricity evolution and appears to osculate outside of the low-order eccentricity-type 2:1 MMR. It is interesting that the secular evolution timescales are rather short, of the order of $\sim$120 yr. Therefore, future observations might be sensitive to transit depth variations. Furthermore, TOI-2525b may soon become a nontransiting planet (different timescales are possible within the mutually inclined posteriors).

5. Discussion

5.1. Dynamical State of the System

Our numerical orbital analysis of the system's configuration revealed that the TOI-2525 pair of planets is outside of the 2:1 MMR. However, the posterior of the apsidal alignment angle $\Delta\omega$ shows bimodality with approximately equal fractions exhibiting libration and circulation. Thus, we took a closer look

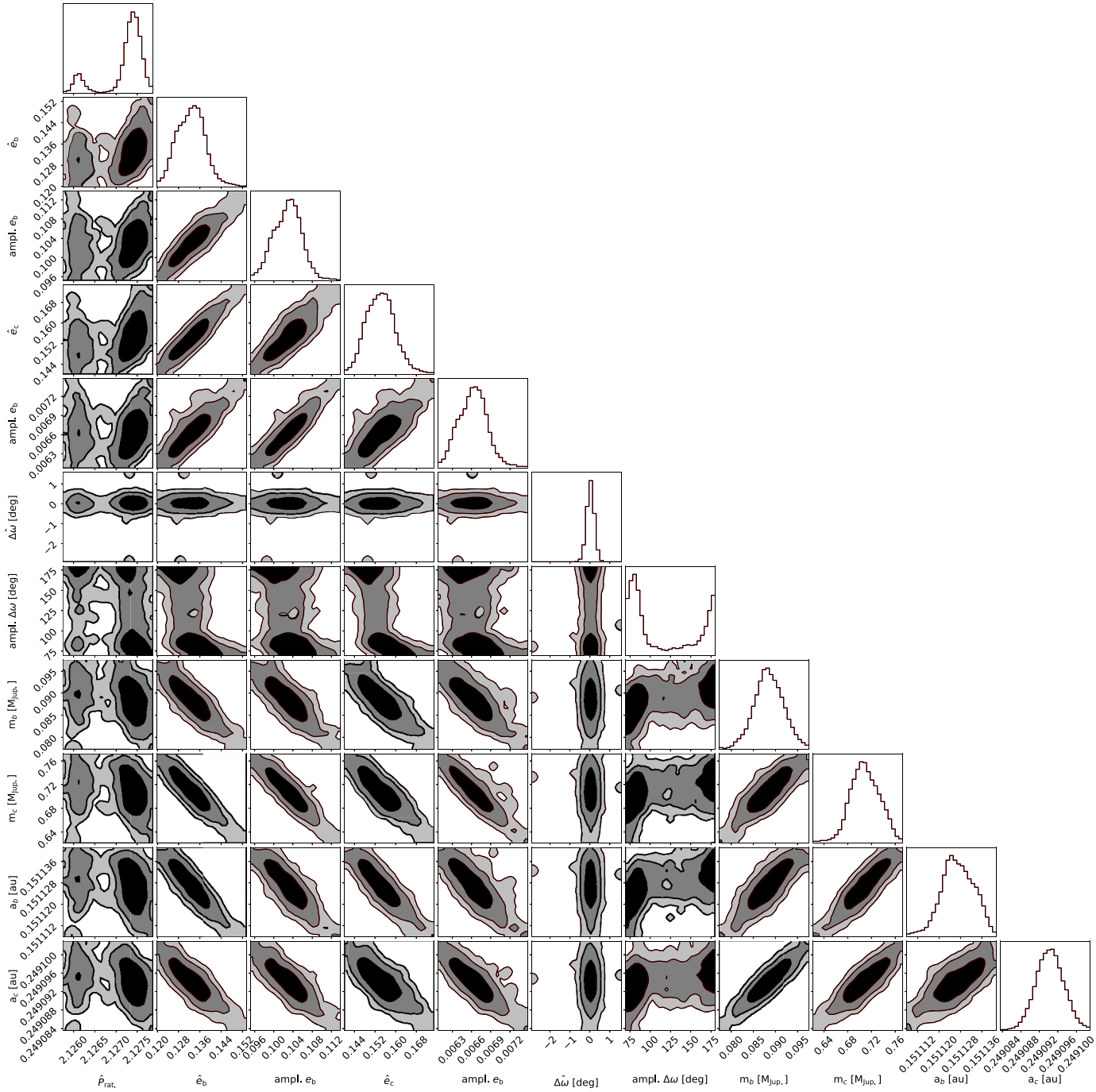

Figure 6. Posteriors of the dynamical properties at the 2:1 period ratio commensurability of the two-planet system TOI-2525. The posteriors are generated by randomly drawing 10,000 samples from the TTV+RV dynamical model. Each sample is tested for stability, and the overall dynamical properties are evaluated at the 2:1 period ratio commensurability. The derived dynamical parameters are the mean period ratio $\hat{P}_{\rm rat.}$; mean eccentricities $\hat{e}_{\rm b}$ and $\hat{e}_{\rm c}$; mean orbital alignment $\Delta\hat{\omega}$; peak-to-peak amplitudes ampl. $e_{\rm b}$, ampl. $e_{\rm c}$, and ampl. $\Delta\omega$; and the planetary dynamical masses and semimajor axes. Note that the posterior distributions of θ_1 and θ_2 are not shown, since these exhibit circulation between 0° and 360°. The black contours on the 2D panels represent the 1σ, 2σ, and 3σ confidence level of the overall posterior samples.

at the dynamical evolution of these two populations. The top and bottom panels of Figure 8 show the characteristic evolution of $\Delta\omega$ for the same stable configuration as in Figure 7 (i.e., our best TTV+RV fit) and a random posterior fit with $\Delta\omega$ in circulation, respectively. The left panels of Figure 8 show $\Delta\omega$ as a function of time, whereas the right panels show the trajectory in the polar plot of $e_b e_c \cos\Delta\omega$ versus $e_b e_c \sin\Delta\omega$. In both cases, the polar plot shows that the system circulates around a point along the positive $e_b e_c \cos\Delta\omega$ axis, i.e., an aligned configuration. For the best fit shown in the top panels, the trajectory in the polar plot is just small enough to miss the origin, and $\Delta\omega$ exhibits large-amplitude libration about 0°. For the example shown in the bottom panels, the trajectory in the polar plot is just large enough to touch the origin, which leads to brief episodes of circulation of $\Delta\omega$. Thus, the bimodality of the apsidal alignment angle is simply due to slightly different sizes of the trajectories in the secular polar variables.

We ruled out a 2:1 MMR librating configuration of the system based on the orbital posterior probability distribution constructed from the available transit and RV data. Similar to

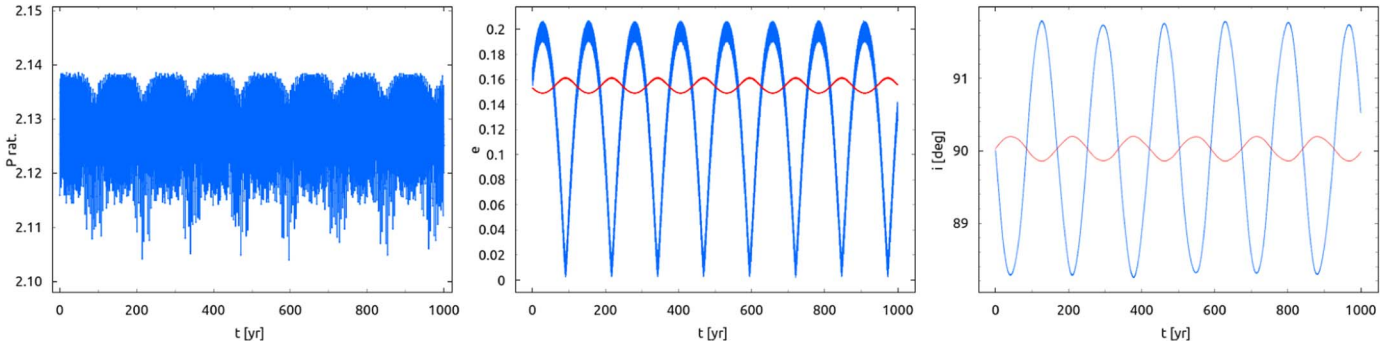

Figure 7. Orbital evolution of the TOI-2525 system for a 1000 yr long *N*-body integration using the Wisdom–Holman scheme. The left panel shows the evolution of the planetary periods, the middle panel shows the eccentricities e_b (blue) and e_c (red) of the best-fit *N*-body model, and the right panel shows the evolution of the line-of-sight inclinations i_b (blue) and i_c (red).

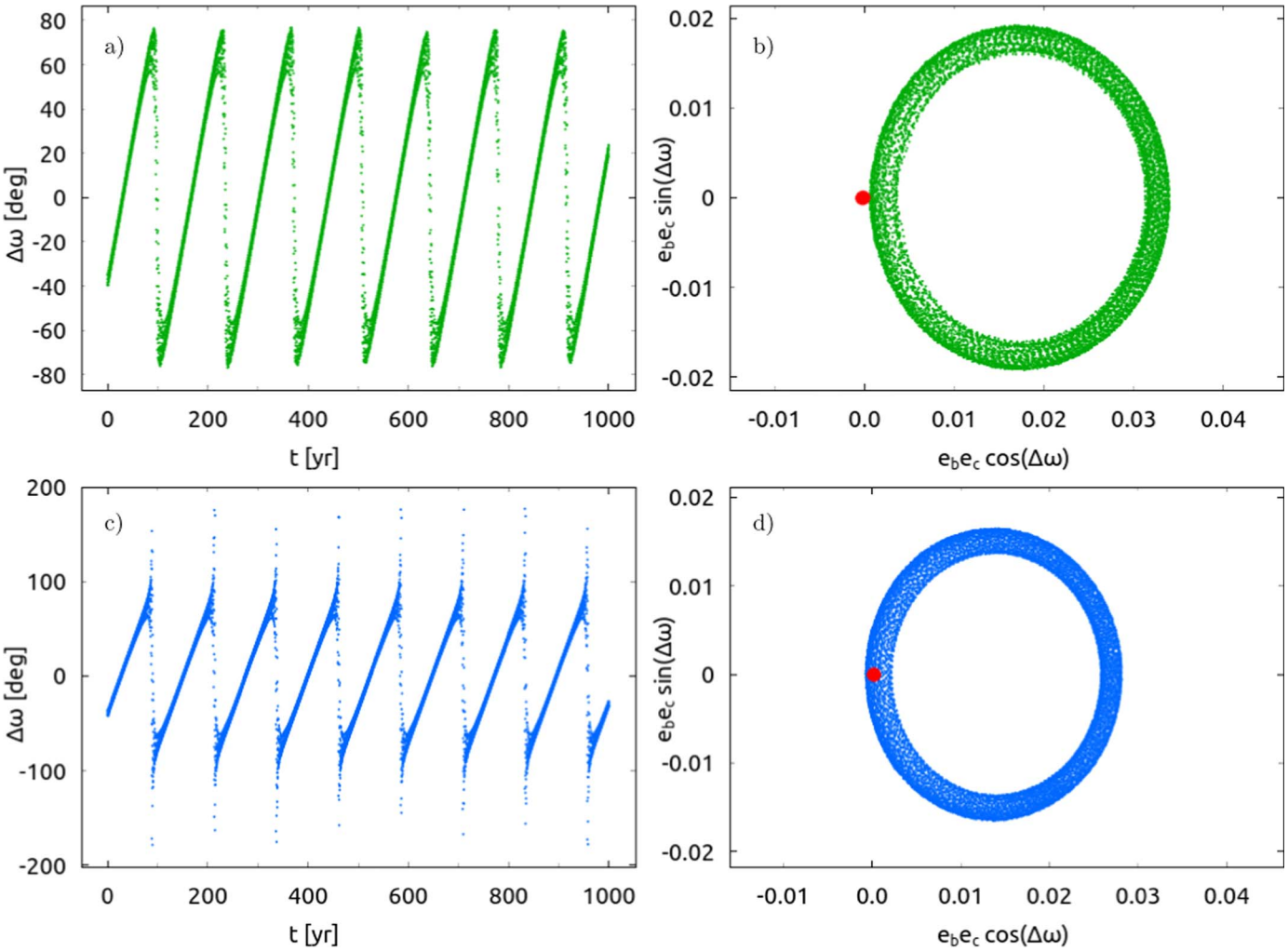

Figure 8. The top panels are the same as in Figure 7 but for the evolution of the apsidal angle $\Delta\omega = \omega_b - \omega_c$ and the trajectory evolution as a function of e_b e_c times the sine/cosine of $\Delta\omega$, respectively. The trajectory just misses the origin (red dot, centered at [0,0]), which leads to libration of $\Delta\omega$ with a semiamplitude of $\sim 80°$. The bottom panels are the same as the top panels but for a random posterior fit that exhibits circulation of $\Delta\omega$ (see Figure 6). The trajectory evolution in this case passes through the origin, which leads to brief episodes of circulation of $\Delta\omega$.

the TOI-2202 system, the osculating period ratio of the TOI-2525 pair of planets is well above 2, consistent with the prominent peak of period ratios of planet pairs observed by the Kepler mission (Lissauer et al. 2011; Fabrycky et al. 2014). Figure 9 shows an analytical analysis of the resonant and near-resonant dynamics in the 2:1 commensurability, following Nesvorný & Vokrouhlický (2016). The constant δ is an orbital invariant that defines the position of the system relative to the 2:1 period ratio, ψ is a combination of the resonant angles θ_1 and θ_2, and the variable Ψ is a combination of planetary masses, semimajor axes, and eccentricities (see Nesvorný & Vokrouhlický 2016 for details). Figure 9 is an updated version of Figure A1 of Trifonov et al. (2021), which now includes the position of TOI-2525, in addition to

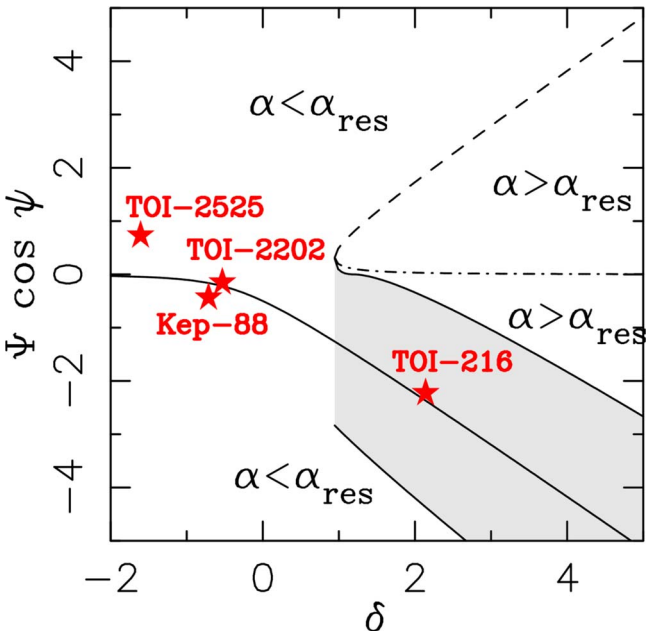

Figure 9. The 2:1 MMR structure diagram following Nesvorný & Vokrouhlický (2016). Four planetary systems are plotted: TOI-2525 (this work), TOI-2202 (Trifonov et al. 2021), TOI-216 (Dawson et al. 2021), and Kepler-88 (Nesvorný et al. 2013). The separatrices and stable point are solid. The dashed line is the unstable point, and the dotted–dashed line is the stable point. See Nesvorný & Vokrouhlický (2016) for more explanations.

TOI-2202 (Trifonov et al. 2021), TOI-216 (Dawson et al. 2021), and Kepler-88 (Nesvorný et al. 2013). The median posterior probability values of TOI-2525, listed in Table 4, lead to $\delta \simeq -1.60$; therefore, the system is firmly outside the libration region, together with the Kepler-88 and TOI-2525 systems. The only system that is in a 2:1 MMR is TOI-216 (see Dawson et al. 2021 for details).

5.2. Possible Formation Mechanisms

An interesting question is how frequently state-of-the-art planet formation models produce systems like TOI-2525, TOI-2202, or TOI-216 and what drives their formation. We explored the abundance and origins of systems with multiple giant planets in synthetic planet populations from the Generation III Bern model (Emsenhuber et al. 2021a; Schlecker et al. 2021a; Emsenhuber et al. 2021b; Schlecker et al. 2021b; Burn et al. 2021; Mishra et al. 2021). The model includes the mechanisms relevant for the dynamical evolution of multi-planet systems, in particular types I and II planet migration (Paardekooper et al. 2011; Dittkrist et al. 2014), eccentricity and inclination damping through planet–disk interaction (Cresswell & Nelson 2008), and dynamical evolution modeled via an *N*-body integrator (Chambers 1999). The planet population with a $0.7\,M_{\odot}$ host star introduced in Burn et al. (2021) is most suitable for the comparison with the K dwarf system presented here. Out of its 999 systems, 92 contain planets more massive than $30\,M_{\oplus}$. We find 51 systems with more than one such planet within orbital periods of 1000 days in the population, typically around host stars with enhanced metallicity. Only a single system includes a pair of warm giant planets in an MMR-like configuration; it contains three giant planets with periods of 48.0, 96.5, and 479.8 days.

The system emerged from a numerical disk with a large solid material content, which is reflected in a high dust-to-gas ratio of 0.024 as compared to the population median of 0.014. This led to efficient core growth and runaway gas accretion of three protoplanets. Through simultaneous inward migration and gravitational interaction, the two warm gas giants were eventually captured in an MMR, a configuration that persisted until the end of the *N*-body integration at 20 Myr. This comparison proposes that the TOI-2525 system was formed in a similar metal-enriched disk. Thus, TOI-2525 is in a configuration whose realization through core accretion is rare but possible, according to the simulations.

We note that the literature contains other examples of pairs of warm Jovian planets that have been extensively studied, for instance, the Kepler-9 system, consisting of a G dwarf star orbited by a mini-Saturn planet pair in a 2:1 MMR (Holman et al. 2010). Other examples include the HD 82943 (Tan et al. 2013) and TIC 279401253 (Bozhilov et al. 2023) systems, both of which are G dwarf stars with almost identical 2:1 MMR Jovian-mass planet pairs. Although rare, M dwarfs have also been found to host 2:1 MMR warm massive systems, with the GJ 876 multiple-planet system (Rivera et al. 2010; Millholland et al. 2018; Trifonov et al. 2018) being widely considered as a benchmark for planetary dynamics and planet formation. The formation of such systems may not depend on the stellar type, but its occurrence rate remains an important observable to be further studied.

5.3. TOI-2525b: A Very Low Density Planet

Objects TOI-2525b and c are two warm, low-density giant planets, a category of planetary systems whose frequency is steadily growing in the literature. The estimated mean density of TOI-2525c of $\rho_{\rm c} = 1.014^{+0.084}_{-0.076}$ g cm^{-3} is lower than that of Jupiter ($\rho_{\rm Jup} = 1.33$ g cm^{-3}) but higher than that of Saturn ($\rho_{\rm Sat} = 0.69$ g cm^{-3}). Therefore, the density of the Jovian-mass planet TOI-2525c is not surprising. The Neptune-mass planet TOI-2525b, however, has a mean density of $\rho_{\rm b} = 0.174^{+0.016}_{-0.015}$ g cm^{-3}, which makes it among the lowest-density Neptune-mass planets known to date. The density of TOI-2525b is a bit larger than the Kepler-51 b, c, and d "super puffs" (Steffen et al. 2013; Masuda 2014) and is comparable to low-density planets like WASP-107 b (Rubenzahl et al. 2021), WASP-131 b, WASP-139 b (Hellier et al. 2017), WASP-21 b (Barros et al. 2011; Ciceri et al. 2013), and HATS-46b b (Brahm et al. 2018), among others. We use the mass–radius models of Fortney et al. (2007) to infer the core mass of planets TOI-2525b and c given the estimated masses, radii, and stellar parameters. We calculate core masses of 6.9 ± 1.4 and 36.6 ± 9.3 $M_{\oplus}$ for TOI-2525b and c, respectively. The ratio of core mass to total mass Zp is therefore $Zp_b = 0.25 \pm 0.05$ and $Zp_c = 0.17 \pm 0.04$.

Figure 10 shows a mass–radius plot for all known transiting planets with measured masses validated by TTVs or RVs. Figure 10 is limited to the giant planets in the range of 0.05–11 $M_{\rm Jup}$ and 0.15–3.0 $R_{\rm Jup}$. Panel (a) of Figure 10 is color-coded with the planetary equilibrium temperature ($T_{\rm eq}$), whereas panel (b) is color-coded with the planetary density. In both panels, we plot an interpolated model for the mass–radius relationship assuming the estimated luminosity of TOI-2525, semimajor axis = 0.2 au, and an age of 3.1 Gyr from Fortney et al. (2007). From Figure 10, it is clear that the higher the $T_{\rm eq}$ of the planet, the larger the radius. Except for the massive planets with a few Jupiter masses or more, the larger radius correlates with low planetary density. Object TOI-2525c is consistent with the

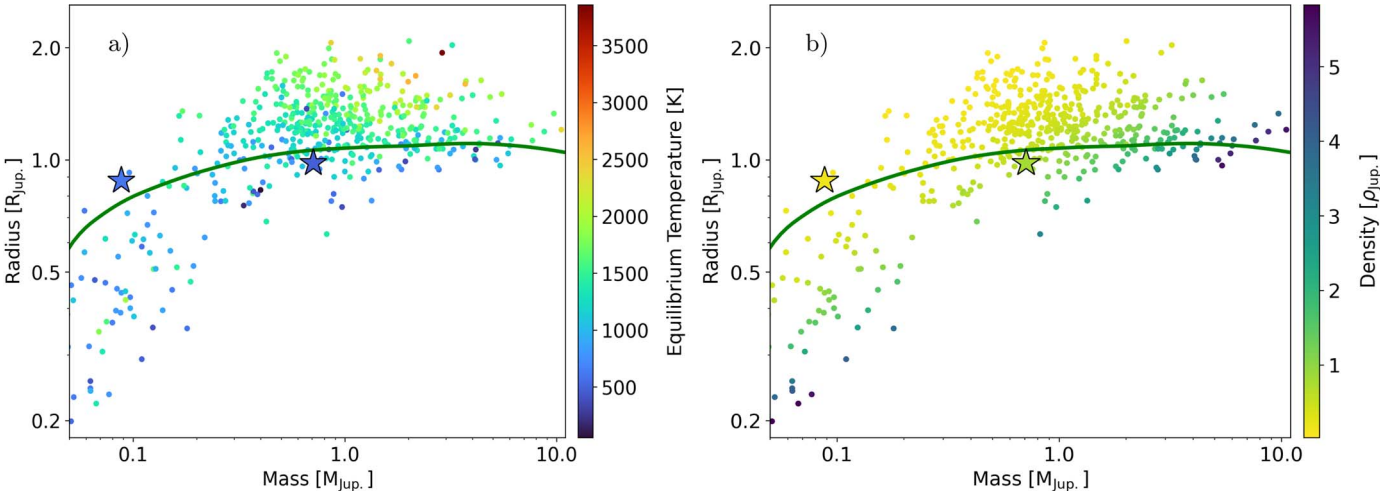

Figure 10. Radius–mass demographics for all giant transiting planets with measured masses by TTVs or RVs. The positions of TOI-2525b and c are plotted with stars. Panel (a) shows the mass–radius relation color-coded by T_{eq}. Panel (b) is the same as panel (a) but color-coded with the planetary density. The solid curve corresponds to the predicted radius using the models of Fortney et al. (2007) given the estimated luminosity of TOI-2525, a semimajor axis = 0.2 au, and an age of 3.1 Gyr.

mass–radius model from Fortney et al. (2007); TOI-2525b is consistent with a large radius, and its mean density is among the lowest for the Neptune-mass planets.

We also model the evolution of both planets in the system, using CEPAM (Guillot & Morel 1995; Guillot et al. 2006) and a nongray atmosphere (Parmentier et al. 2015), to provide constraints on their interiors. We assume simple structures consisting of a central dense core surrounded by a hydrogen and helium envelope of solar composition. The core is assumed to be made of 50% ices and 50% rocks. Figure 11 shows the resulting evolution models. The core mass of TOI-2525c is found to be between 20 and 43 $M_\oplus$. This indicates that the enrichment in heavy elements of TOI-2525c could be comparable to Jupiter's, which is between 8 and 46 $M_\oplus$ (Guillot et al. 2022). With a radius similar to Saturn's (1.08 times larger) but 3.4 times less massive than Saturn, TOI-2525b is an uncommon example of a very low density and inflated planet with an equilibrium temperature close to 500 K. The H–He envelope of TOI-2525b is found to be between 19 and 24 $M_\oplus$. The case of TOI-2525b is challenging for the traditional core accretion formation scenario. With our simple modeling of TOI-2525b, such a small envelope hints that the accretion of H–He has potentially been hindered. Characterizing the atmospheres of both planets of the system would be very useful to understand their structure and formation.

Not many inflated Neptune-mass planets are known, making TOI-2525b a useful addition to the sample of transiting planets with a measured mass. The low density, and thus large scale height, of TOI-2525b makes it a good target for a future atmospheric investigation with transmission spectroscopy.

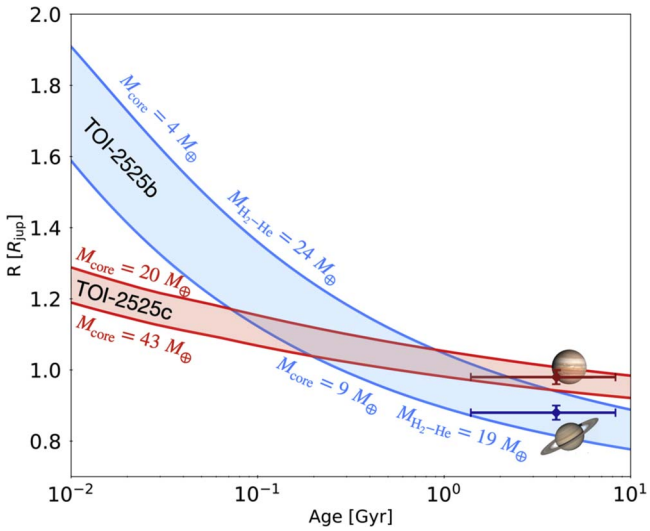

Figure 11. Evolution models of TOI-2525b and c. All models assume a central ice–rock core surrounded by a hydrogen–helium envelope of solar composition. For both planets, the range of core masses is shown. For TOI-2525b, the range of envelope masses is also shown. The error bars correspond to observational constraints on their age and radius compared to the ones of Jupiter and Saturn.

6. Summary and Conclusions

We report the discovery of a warm pair of giant planets around a K dwarf star uncovered by TESS with multisector light-curve photometry. The TOI-2525 light curve shows recurrent transit events consistent with two gravitationally interacting giant planets resulting in a robust TTV signal with a semiamplitude of ~6 hr for the inner planet. We obtained precise spectroscopic Doppler follow-up with FEROS and PFS to estimate the stellar parameters and constrain the planetary masses. Using high signal-to-noise ratio FEROS spectra of TOI-2525, we estimate a stellar mass of $M_\star = 0.849^{+0.024}_{-0.033}\ M_\odot$ and a stellar radius of $R_\star = 0.785^{+0.007}_{-0.007}\ R_\odot$. Using this stellar mass and radius, we conducted an extensive orbital analysis of the TESS TTVs and RVs using self-consistent *N*-body models. This analysis allowed us to construct an accurate orbital model from which we predicted future transit events, confirmed by follow-up photometry observations by ASTEP, OM-SSO, and LCOGT.

The complete collection of RVs and transit light curves allowed us to perform more extensive joint TTV+RV analyses, as well as light-curve photodynamical+RV *N*-body orbital modeling. We found that TOI-2525b is a massive Neptune with a dynamical mass of $m_b = 0.088^{+0.005}_{-0.005}\ M_{Jup}$ and radius of $R_b = 0.88^{+0.02}_{-0.02}\ R_{Jup}$. Thus, the estimated density of TOI-2525b is $\rho_b = 0.174^{+0.016}_{-0.015}$ g cm^{-3}, which makes it among the lowest-density Neptune-mass planets known to date, similar to the Kepler-51 planets. The outer transiting planet, TOI-2525c, is a

Jovian-mass planet with $m_c = 0.709^{+0.034}_{-0.034}$ M_{Jup} and planetary radius $R_c = 0.98^{+0.02}_{-0.02}$ R_{Jup} and, therefore, a relatively low mean density of $\rho_c = 1.014^{+0.084}_{-0.076}$ g cm^{-3}.

The warm pair of massive planets is near the 2:1 period ratio commensurability with orbital periods of $P_b = 23.288^{+0.001}_{-0.002}$ and $P_c = 49.260^{+0.001}_{-0.001}$ days, but the dynamics of the system clearly suggest that it is outside the MMR dynamical configuration.

The TOI-2525 system is very similar to other K dwarf TESS systems; TOI-2202 and TOI-216 are composed of almost identical K dwarf primaries and two warm giant planets near the 2:1 MMR. These three systems will be a useful sample for studying the formation and composition of warm giant pairs around K dwarf stars.

This research has made use of the Exoplanet Follow-up Observation Program website, which is operated by the California Institute of Technology, under contract with the National Aeronautics and Space Administration under the Exoplanet Exploration Program. Funding for the TESS mission is provided by NASA's Science Mission directorate. This paper includes data collected by the TESS mission, which are publicly available from the Mikulski Archive for Space Telescopes (MAST). Some of the data presented in this paper were obtained from MAST. The specific observations analyzed can be accessed via doi:10.17909/fwdt-2x66. This research made use of exoplanet (Foreman-Mackey et al. 2021, 2021) and its dependencies (Astropy Collaboration et al. 2013; Kipping 2013; Salvatier et al. 2016; Theano Development Team 2016; Foreman-Mackey et al. 2017a; Astropy Collaboration et al. 2018; Foreman-Mackey 2018; Kumar et al. 2019). Resources supporting this work were provided by the NASA High-End Computing (HEC) Program through the NASA Advanced Supercomputing (NAS) Division at Ames Research Center for the production of the SPOC data products. This work makes use of observations from the LCOGT network. Part of the LCOGT telescope time was granted by NOIRLab through the Mid-Scale Innovations Program (MSIP). MSIP is funded by NSF. This work makes use of observations from the ASTEP telescope. ASTEP benefited from the support of the French and Italian polar agencies IPEV and PNRA in the framework of the Concordia station program, from INSU, ESA and the University of Birmingham. T.T. acknowledges support by the DFG Research Unit FOR 2544 "Blue Planets around Red Stars" project No. KU 3625/2-1. T.T. further acknowledges support by the BNSF program "VIHREN-2021" project No. К П-06-Д/5. M.H.L. was supported in part by Hong Kong RGC grant HKU 17305618. A.J., R.B., M.H., and F.R. acknowledge support from ANID—Millennium Science Initiative—ICN12_009. A.J. acknowledges additional support from FONDECYT project 1210718. R.B. acknowledges support from FONDECYT project 11200751. M.N.G. acknowledges support from the European Space Agency (ESA) as an ESA Research Fellow. The results reported herein benefited from collaborations and/or information exchange within the program "Alien Earths" (supported by the National Aeronautics and Space Administration under agreement No. 80NSSC21K0593) for NASA's Nexus for Exoplanet System Science (NExSS) research coordination network sponsored by NASA's Science Mission Directorate. This research is funded in part by the European Union's Horizon 2020 research and innovation program (grant agreement No. 803193/BEBOP) and the Science and Technology Facilities Council (STFC; grant No. ST/S00193X/1).

Facilities: TESS, MPG-2.2 m/FEROS, Magellan-6.5 m/PFS, LCOGT.

Software: Exo-Striker (Trifonov 2019), exoplanet (Foreman-Mackey et al. 2021), CERES (Brahm et al. 2017a), ZASPE (Brahm et al. 2017b), TESSERACT (F.Rojas 2023, in preparation), TESSCut (Brasseur et al. 2019), lightkurve (Lightkurve Collaboration et al. 2018), emcee (Foreman-Mackey et al. 2013), corner.py (Foreman-Mackey 2016), dynesty (Speagle 2020), batman(Kreidberg 2015), celerite (Foreman-Mackey et al. 2017b), TTVfast (Deck et al. 2014), wotan (Hippke et al. 2019), transitleastsquares (Hippke & Heller 2019), pyExoRaMa (Francesco et al. 2022), AstroImageJ (Collins et al. 2017).

Appendix

Table A1 is a continuation of Table 3 presented in themain text. Table A1 presents the remaining nuisance parameters used in for the derivations of the TTVs. In Table A2, we list the estimated mid-transit time estimates of TOI-2525b and c (i.e., TTVs), and in Table A3, we list the estimated posterior probability distribution of our joint Doppler and transit light-curve photodynamical model with `flexifit`. Figure A1 shows the posterior probability distribution of the joint Doppler and TTV modeling with EXO-STRIKER, Figures A2 and A3 show the `flexifit` model applied to the available transit light curves, and Figure A4 shows the MCMC posterior probability distribution of the `flexifit` joint photodynamical analysis.

Table A1
Parameters of the Two-planet System TOI-2525, Its Host Star, and the Light Curves Derived during TTV Extraction (Continued from Table 3)

Parameter	Median	σ
$\mu_{\rm TESS-LC}$	−0.0003	0.0004
$\log(\rho)_{\rm TESS-LC}$	0.830	0.093
$\log(\sigma)_{\rm TESS-LC}$	−5.628	0.056
$\mu_{\rm TESS-SC}$	0.0000	0.0001
$\log(\rho)_{\rm TESS-SC}$	0.526	0.156
$\log(\sigma)_{\rm TESS-SC}$	−7.246	0.058
$\mu_{\rm ASTEP1}$	0.0002	0.0001
$\beta_{\rm ASTEP1}$	0.0054	0.002
$\mu_{\rm ASTEP2}$	0.0000	0.0001
$\beta_{\rm ASTEP2}$	−0.001	0.002
$\mu_{\rm ASTEP3}$	0.0000	0.0002
$\beta_{\rm ASTEP3}$	−0.005	0.005
$\mu_{\rm ASTEP4}$	0.0006	0.0002
$\beta_{\rm ASTEP4}$	0.0185	0.005
$\mu_{\rm ASTEP5}$	−0.0001	0.0001
$\beta_{\rm ASTEP5}$	−0.004	0.002
$\mu_{\rm ASTEP6}$	−0.0001	0.0001
$\beta_{\rm ASTEP6}$	−0.004	0.0008
$\mu_{\rm SSO}$	−0.0007	0.0003
$\beta_{\rm SSO}$	−0.008	0 006
$\mu_{\rm CTIOi}$	0.0030	0.0002
$\beta_{\rm CTIOi}$	−0.0061	0.0081
$\mu_{\rm CTIOg}$	0.0031	0.0002
$\beta_{\rm CTIOg}$	−0.0404	0.0105
$\mu_{\rm CTIOi2}$	0.0047	0.0001
$\beta_{\rm CTIOi2}$	−0.0024	0.0039
$u_{0,\rm TESS}$	0.502	0.150
$u_{1,\rm TESS}$	0.422	0.189
$u_{0,\rm ASTEP}$	0.409	0.072
$u_{1,\rm ASTEP}$	−0.159	0.069
$u_{0,\rm SSO}$	0.528	0.220
$u_{1,\rm SSO}$	0.053	0.299
$u_{0,\rm SAAO,g}$	0.688	0.330
$u_{1,\rm SAAO,g}$	−0.055	0.348
$u_{0,\rm SAAO,i}$	0.403	0.143
$u_{1,\rm SAAO,i}$	0.057	0.220

Note. TESS-LC/SC means long- (30 minutes) and short- (2 minutes) cadence data, respectively. The μ values correspond to the fitted mean of each light-curve set, while the β values correspond to the coefficient of a linear trend in units of day^{-1}. The $\{u_0, u_1\}$ coefficients correspond to the coefficients of a quadratic limb-darkening law as derived for each instrument/band, as indicated in the subscript for each coefficient.

Table A2
Individual Mid-transit Time Estimates of TOI-2525b Extracted from TESS, ASTEP, SSO, and LCOGT Used for TTV Analysis

N Transit	t_0 (BJD)	σ t_0 (BJD)	Instrument
	Planet b		
1	2,458,333.527	0.005	TESS
4	2,458,403.441	0.002	TESS
5	2,458,426.775	0.007	TESS
6	2,458,450.130	0.011	TESS
7	2,458,473.508	0.008	TESS
8	2,458,496.853	0.003	TESS
9	2,458,520.237	0.004	TESS
11	2,458,566.956	0.002	TESS
15	2,458,659.976	0.009	TESS
32	2,459,056.051	0.006	TESS
33	2,459,079.266	0.003	TESS
35	2,459,125.641	0.003	TESS
36	2,459,148.834	0.003	TESS
38	2,459,195.308	0.004	TESS
39	2,459,218.599	0.004	TESS
41	2,459,265.237	0.003	TESS
42	2,459,288.598	0.003	TESS
43	2,459,311.952	0.003	TESS
45	2,459,358.682	0.004	TESS
50	2,459,475.305	0.004	ASTEP
55	2,459,591.328	0.002	LCOGT-SAAO
	Planet c		
1	2,458,335.410	0.004	TESS
2	2,458,384.648	0.002	TESS
3	2,458,433.866	0.006	TESS
4	2,458,483.090	0.007	TESS
8	2,458,680.073	0.005	TESS
17	2,459,123.270	0.003	TESS
19	2,459,221.791	0.003	TESS
21	2,459,320.238	0.002	ASTEP
22	2,459,369.454	0.003	ASTEP
24	2,459,467.906	0.003	ASTEP
25	2,459,517.190	0.003	SSO

Table A3
MCMC Posterior Medians, Best Fits, and Adopted Priors from Orbital Elements, Offset, and Jitter Terms from `flexifit`

Parameter	Median and 1σ	Best Fit	Adopted Prior
TOI-2525b			
Period P (days)	$23.2856^{+0.0017}_{-0.0017}$	23.2865	$\mathcal{U}$(23.1,23.4)
Mass m ($M_{\rm Jup}$)	$0.084^{+0.005}_{-0.005}$	0.086	$\mathcal{U}$(10,100 $M_\oplus$)
Eccentricity e	$0.170^{+0.011}_{-0.010}$	0.167	$\mathcal{U}$(0,0.45)
Longitude of periastron ω (deg)	$345.9^{+0.8}_{-0.8}$	345.7	$\mathcal{U}$(0,360)
Time of conjunction $t_{\rm conj}$ (BJD –2,457,000)	$1333.5289^{+0.0020}_{-0.0020}$	1333.5293	$\mathcal{U}$(1333.52,1356.82)
Inclination i (deg)	$89.50^{+0.07}_{-0.07}$	89.47	$\mathcal{U}$(80,100)
Planet-to-star radius ratio R_p/R_s	$0.1013^{+0.0008}_{-0.0008}$	0.1009	$\mathcal{U}$(0.001,0.2)
Longitude of ascending node Ω (deg)	0 (fixed)	0 (fixed)	(fixed)
Radius R_p ($R_{\rm Jup}$)	$0.774^{+0.010}_{-0.010}$	0.771	(derived)
Density ρ (g cm^{-3})	$0.225^{+0.015}_{-0.014}$	0.235	(derived)
Semimajor axis a (au)	$0.1511^{+0.0020}_{-0.0020}$	0.1511	(derived)
Transit duration $t_{\rm dur}$ (hr)	$4.05^{+0.07}_{-0.07}$	4.00	(derived)
RV semiamplitude K (m s^{-1})	$6.7^{+0.4}_{-0.4}$	6.9	(derived)
Mean longitude λ (deg)	$107.8^{+0.8}_{-0.8}$	107.5	(derived)
TOI-2525c			
Period P (days)	$49.2519^{+0.0004}_{-0.0004}$	49.2518	$\mathcal{U}$(49.1,49.4)
Mass m ($M_{\rm Jup}$)	$0.657^{+0.031}_{-0.032}$	0.675	$\mathcal{U}$(100,400 $M_\oplus$)
Eccentricity e	$0.157^{+0.008}_{-0.007}$	0.153	$\mathcal{U}$(0,0.45)
Longitude of periastron ω (deg)	$21.5^{+1.1}_{-1.1}$	21.5	$\mathcal{U}$(0,360)
Time of conjunction $t_{\rm conj}$ (BJD –2,457,000)	$1335.4118^{+0.0014}_{-0.0014}$	1335.4121	$\mathcal{U}$(1333.52,1382.77)
Inclination i (deg)	$89.97^{+0.09}_{-0.07}$	90.03	$\mathcal{U}$(80,100)
Planet-to-star radius ratio R_p/R_s	$0.1183^{+0.0005}_{-0.0005}$	0.1182	$\mathcal{U}$(0.001,0.25)
Longitude of ascending node Ω (deg)	$1.1^{+1.0}_{-0.7}$	0.4	$\mathcal{U}$(−10,10)
Radius R_p ($R_{\rm Jup}$)	$0.904^{+0.010}_{-0.010}$	0.903	(derived)
Density ρ (g cm^{-3})	$1.11^{+0.07}_{-0.07}$	1.14	(derived)
Semimajor axis a (au)	$0.249^{+0.004}_{-0.004}$	0.249	(derived)
Transit duration $t_{\rm dur}$ (hr)	$5.502^{+0.013}_{-0.027}$	5.514	(derived)
RV semiamplitude K (m s^{-1})	$41.2^{+2.2}_{-2.2}$	42.2	(derived)
Mean longitude λ (deg)	$93.2^{+1.1}_{-1.1}$	93.2	(derived)
$\rm RV_{off}$ PFS (m s^{-1})	-7^{+11}_{-11}	−4	$\mathcal{U}(-\infty, \infty)$
$\rm RV_{jit}$ PFS (m s^{-1})	31^{+10}_{-7}	29	$\mathcal{U}(exp(-5), exp(5))$
$\rm TR_{off}$ TESS FFI (ppm)	-310^{+60}_{-60}	−300	$\mathcal{U}(-\infty, \infty)$
$\rm TR_{off}$ TESS PDC (year 3) (ppm)	380^{+60}_{-60}	330	$\mathcal{U}(-\infty, \infty)$
$\rm TR_{off}$ ASTEP 1 (ppm)	390^{+250}_{-260}	320	$\mathcal{U}(-\infty, \infty)$
$\rm TR_{off}$ ASTEP 2 (ppm)	350^{+260}_{-260}	340	$\mathcal{U}(-\infty, \infty)$
$\rm TR_{off}$ ASTEP 3 (ppm)	210^{+310}_{-320}	340	$\mathcal{U}(-\infty, \infty)$
$\rm TR_{off}$ ASTEP 4 (ppm)	650^{+320}_{-330}	940	$\mathcal{U}(-\infty, \infty)$
$\rm TR_{off}$ SSO (ppm)	-1870^{+310}_{-310}	−1850	$\mathcal{U}(-\infty, \infty)$
$\rm TR_{off}$ CTIO (ppm)	6690^{+410}_{-410}	6620	$\mathcal{U}(-\infty, \infty)$
$\rm TR_{off}$ SAAO1 (ppm)	7880^{+350}_{-350}	8000	$\mathcal{U}(-\infty, \infty)$
$\rm TR_{off}$ SAAO2 (ppm)	9140^{+150}_{-150}	9000	$\mathcal{U}(-\infty, \infty)$
$\rm TR_{off}$ ASTEP5 (ppm)	-500^{+160}_{-170}	−580	$\mathcal{U}(-\infty, \infty)$
$\rm TR_{off}$ ASTEP6 (ppm)	-280^{+130}_{-130}	−270	$\mathcal{U}(-\infty, \infty)$

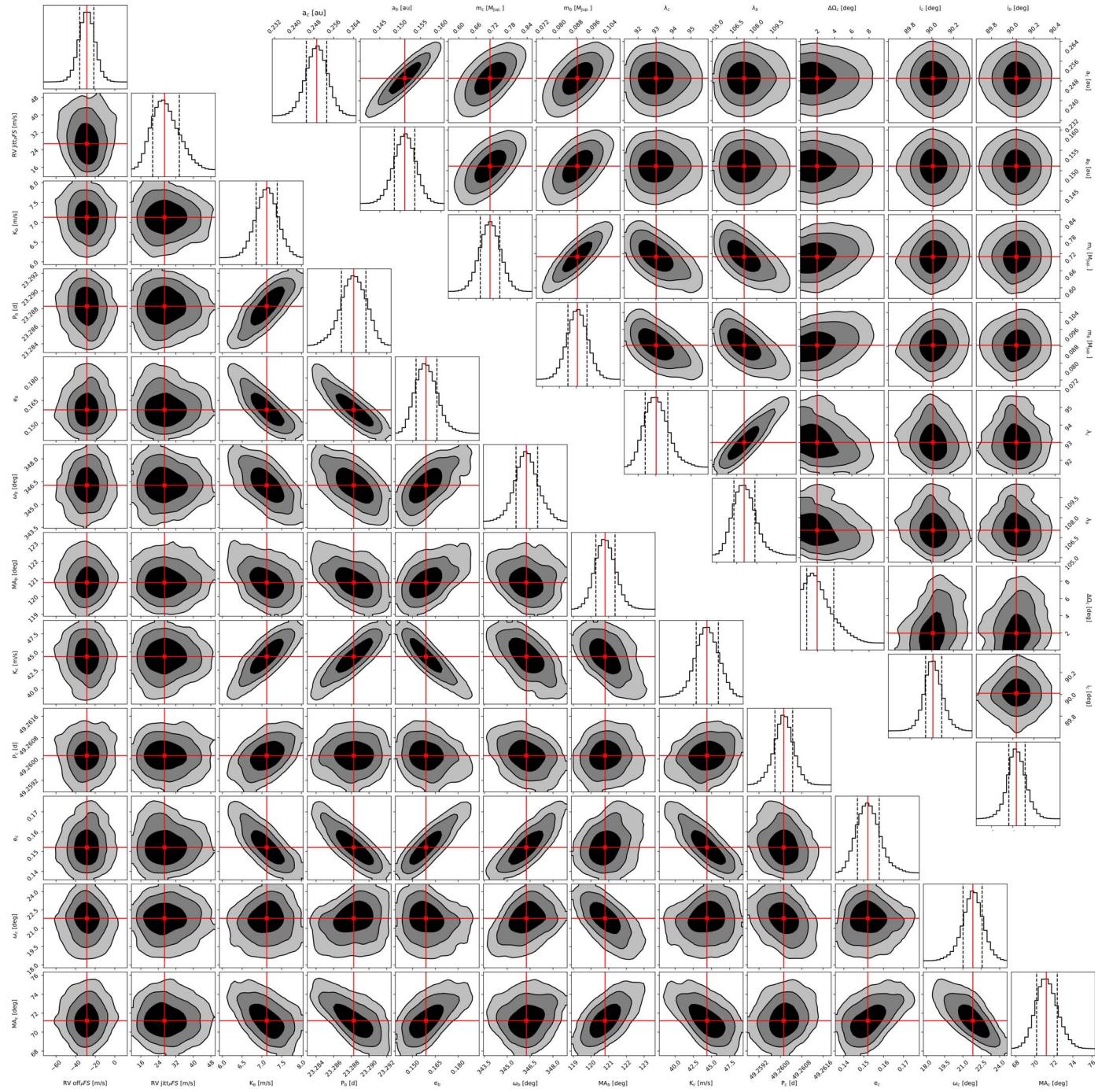

Figure A1. EXO-STRIKER global parameter search results of the TESS, ASTEP, OM-SSO, and LCOGT TTVs of TOI-2525b and c and the Doppler RVs from FEROS and PFS. The posterior probability distribution is achieved with an NS scheme employing a two-planet self-consistent dynamical model. The black contours on the 2D panels represent the 1σ, 2σ, and 3σ confidence levels of the overall posteriors. Red crosses point to the median position of the posterior parameters.

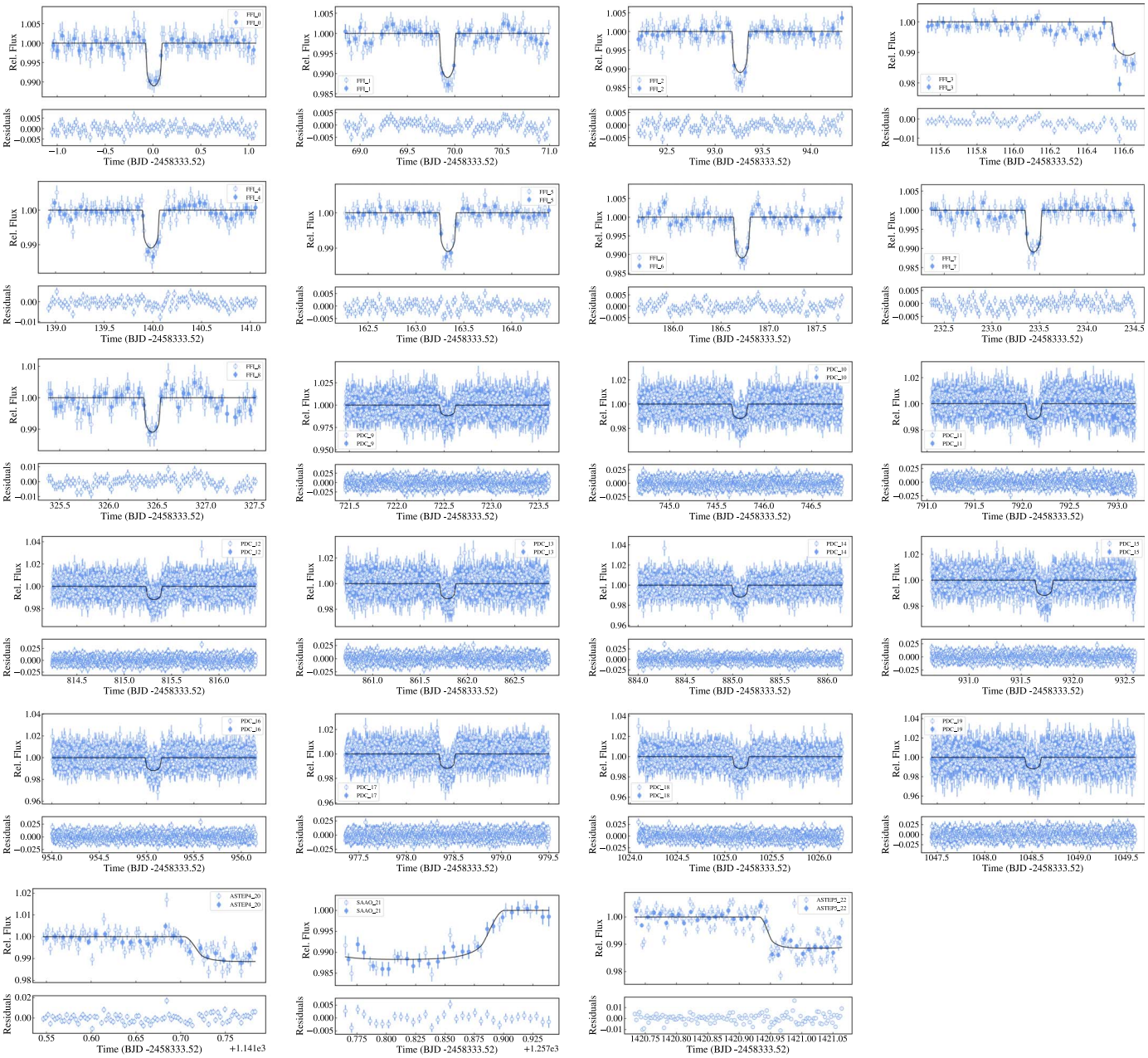

Figure A2. Shown are all transit light curves of TOI-2525b from the photodynamic model observed by different telescopes. Nine of them are TESS observed (FFI), 11 are TESS observed transits (PDCSAP), two transits are observed by ASTEP, and one by SAAO. A 30 minute binning was introduced after the fit with errors calculated by standard deviation (filled circles).

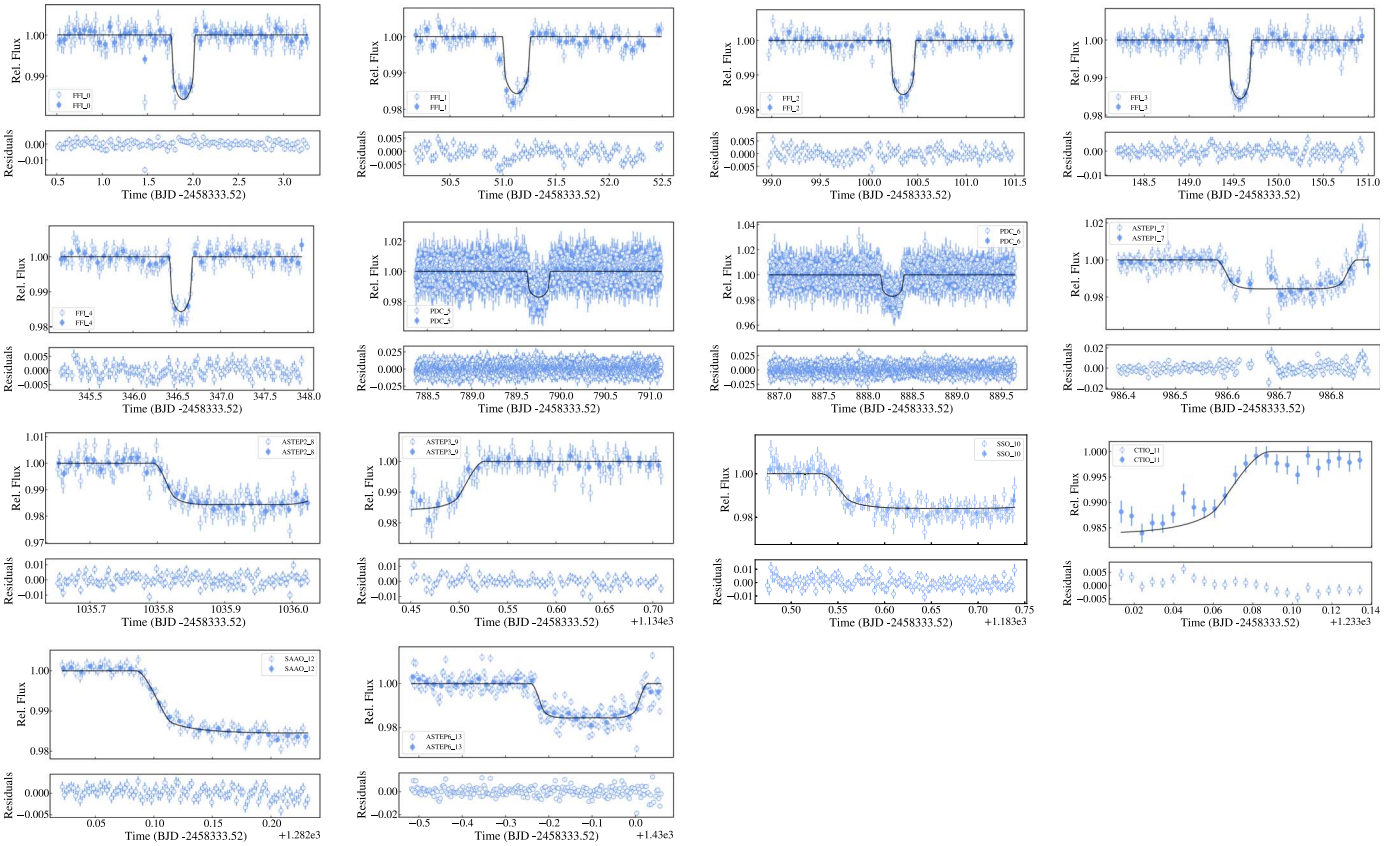

Figure A3. Shown are all transit light curves of TOI-2525c from the photodynamic model observed by different telescopes. Five of them are TESS observed (FFI), three are TESS observed transits (PDCSAP), four transits are observed by ASTEP, one by CTIO, and one by SAAO. A 30 minute binning was introduced after the fit with errors calculated by standard deviation (filled circles).

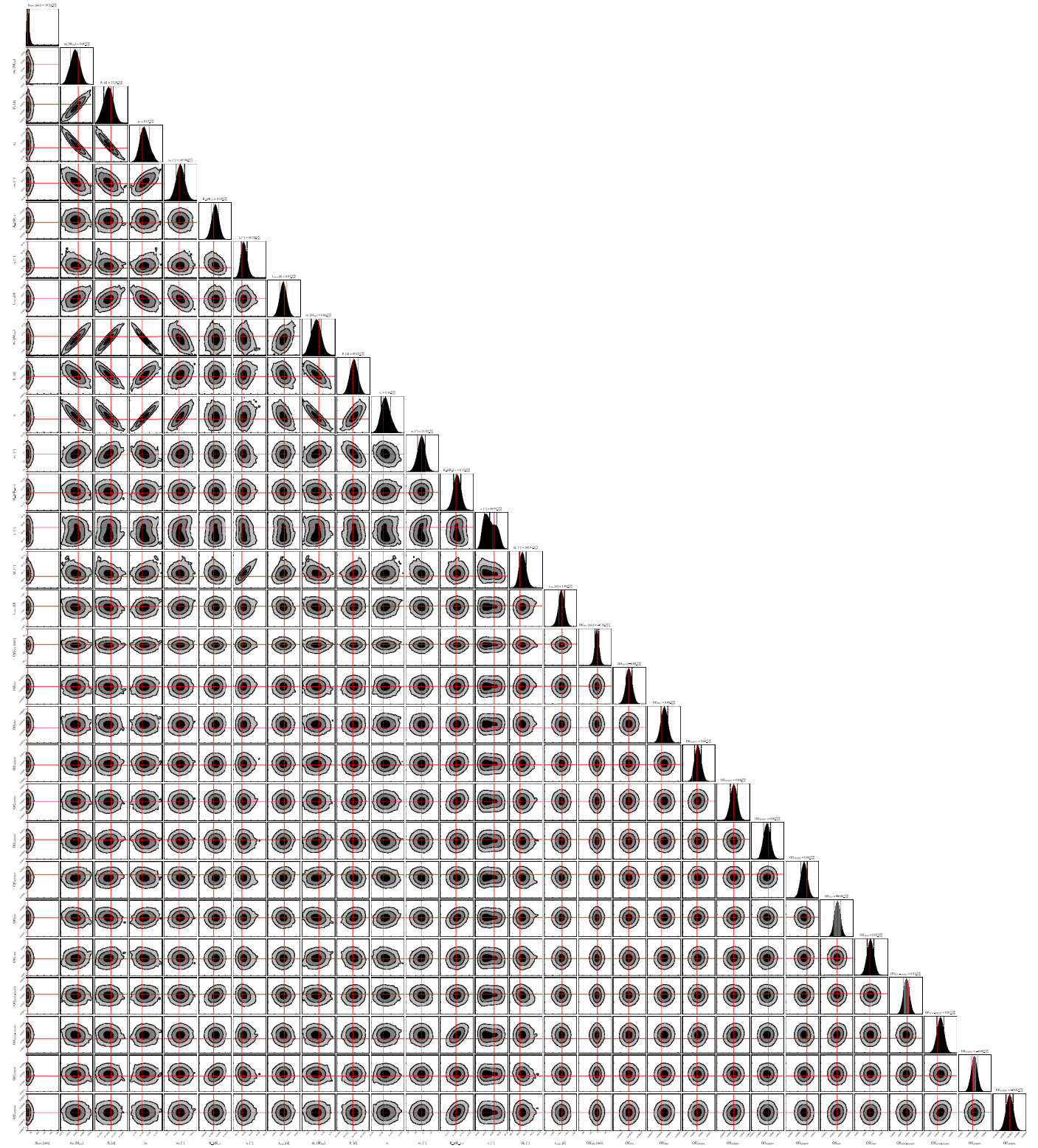

Figure A4. Posterior distribution for the joint photodynamical analysis. The orbital parameters of both planets and jitter and offset terms are obtained by an MCMC analysis in `flexifit` (https://gitlab.gwdg.de/sdreizl/exoplanet-flexi-fit). The best-fit posteriors are marked in red. The scattered black lines represent the median and 1σ intervals of the distribution.

ORCID iDs

Trifon Trifonov https://orcid.org/0000-0002-0236-775X
Rafael Brahm https://orcid.org/0000-0002-9158-7315
Andrés Jordán https://orcid.org/0000-0002-5389-3944
Thomas Henning https://orcid.org/0000-0002-1493-300X
Melissa J. Hobson https://orcid.org/0000-0002-5945-7975
Martin Schlecker https://orcid.org/0000-0001-8355-2107
Saburo Howard https://orcid.org/0000-0003-4894-7271
Nestor Espinoza https://orcid.org/0000-0001-9513-1449

Man Hoi Lee https://orcid.org/0000-0003-1930-5683
David Nesvorny https://orcid.org/0000-0002-4547-4301
Felipe I. Rojas https://orcid.org/0000-0003-3047-6272
Khalid Barkaoui https://orcid.org/0000-0003-1464-9276
Diana Kossakowski https://orcid.org/0000-0002-0436-7833
Stefan Dreizler https://orcid.org/0000-0001-6187-5941
René Heller https://orcid.org/0000-0002-9831-0984
Tristan Guillot https://orcid.org/0000-0002-7188-8428
Amaury H. M. J. Triaud https://orcid.org/0000-0002-5510-8751
Philippe Bendjoya https://orcid.org/0000-0002-4278-1437
Nicolas Crouzet https://orcid.org/0000-0001-7866-8738
Georgina Dransfield https://orcid.org/0000-0002-3937-630X
Thomas Gasparetto https://orcid.org/0000-0002-7913-4866
Maximilian N. Günther https://orcid.org/0000-0002-3164-9086
Djamel Mékarnia https://orcid.org/0000-0001-5000-7292
Olga Suarez https://orcid.org/0000-0002-3503-3617
R. Paul Butler https://orcid.org/0000-0003-1305-3761
Jeffrey D. Crane https://orcid.org/0000-0002-5226-787X
Stephen Shectman https://orcid.org/0000-0002-8681-6136
George R. Ricker https://orcid.org/0000-0003-2058-6662
Avi Shporer https://orcid.org/0000-0002-1836-3120
Roland Vanderspek https://orcid.org/0000-0001-6763-6562
Jon M. Jenkins https://orcid.org/0000-0002-4715-9460
Bill Wohler https://orcid.org/0000-0002-5402-9613
Karen A. Collins https://orcid.org/0000-0001-6588-9574
Kevin I. Collins https://orcid.org/0000-0003-2781-3207
David R. Ciardi https://orcid.org/0000-0002-5741-3047
Thomas Barclay https://orcid.org/0000-0001-7139-2724
Ismael Mireles https://orcid.org/0000-0002-4510-2268
Sara Seager https://orcid.org/0000-0002-6892-6948
Joshua N. Winn https://orcid.org/0000-0002-4265-047X

References

Astropy Collaboration, Robitaille, T. P., Tollerud, E. J., et al. 2013, A&A, 558, A33
Astropy Collaboration, Price-Whelan, A. M., Sipőcz, B. M., et al. 2018, AJ, 156, 123
Baluev, R. V. 2009, MNRAS, 393, 969
Barros, S. C. C., Pollacco, D. L., Gibson, N. P., et al. 2011, MNRAS, 416, 2593
Baruteau, C., Crida, A., Paardekooper, S. J., et al. 2014, in Protostars and Planets VI, ed. H. Beuther et al. (Tucson, AZ: Univ. Arizona Press), 667
Bitsch, B., Trifonov, T., & Izidoro, A. 2020, A&A, 643, A66
Bozhilov, V., Antonova, D., Hobson, M. J., et al. 2023, arXiv:2302.10838
Brahm, R., Espinoza, N., Jordán, A., et al. 2019, AJ, 158, 45
Brahm, R., Hartman, J. D., Jordán, A., et al. 2018, AJ, 155, 112
Brahm, R., Jordán, A., & Espinoza, N. 2017a, PASP, 129, 034002
Brahm, R., Jordán, A., Hartman, J., & Bakos, G. 2017b, MNRAS, 467, 971
Brahm, R., Nielsen, L. D., Wittenmyer, R. A., et al. 2020, AJ, 160, 235
Brasseur, C. E., Phillip, C., Fleming, S. W., Mullally, S. E., & White, R. L. 2019, Astrocut: Tools for creating cutouts of TESS images, Astrophysics Source Code Library, ascl:1905.007
Bressan, A., Marigo, P., Girardi, L., et al. 2012, MNRAS, 427, 127
Brown, T. M., Baliber, N., Bianco, F. B., et al. 2013, PASP, 125, 1031
Burn, R., Schlecker, M., Mordasini, C., et al. 2021, A&A, 656, A72
Butler, R. P., Marcy, G. W., Williams, E., et al. 1996, PASP, 108, 500
Castelli, F., & Kurucz, R. L. 2004, A&A, 405, 1095
Chambers, J. E. 1999, MNRAS, 304, 793
Ciceri, S., Mancini, L., Southworth, J., et al. 2013, A&A, 557, A30
Coleman, G. A. L., & Nelson, R. P. 2014, MNRAS, 445, 479
Collins, K. A., Kielkopf, J. F., Stassun, K. G., & Hessman, F. V. 2017, AJ, 153, 77
Crane, J. D., Shectman, S. A., & Butler, R. P. 2006, Proc. SPIE, 6269, 626931
Crane, J. D., Shectman, S. A., Butler, R. P., et al. 2010, Proc. SPIE, 7735, 773553
Crane, J. D., Shectman, S. A., Butler, R. P., Thompson, I. B., & Burley, G. S. 2008, Proc. SPIE, 7014, 701479
Cresswell, P., & Nelson, R. P. 2008, A&A, 482, 677
Dawson, R. I., Huang, C. X., Brahm, R., et al. 2021, AJ, 161, 161
Deck, K. M., Agol, E., Holman, M. J., & Nesvorný, D. 2014, ApJ, 787, 132
Dittkrist, K. M., Mordasini, C., Klahr, H., Alibert, Y., & Henning, T. 2014, A&A, 567, A121
Dong, J., Huang, C. X., Dawson, R. I., et al. 2021, ApJS, 255, 6
Dumusque, X., Turner, O., Dorn, C., et al. 2019, A&A, 627, A43
Emsenhuber, A., Mordasini, C., Burn, R., et al. 2021a, A&A, 656, A69
Emsenhuber, A., Mordasini, C., Burn, R., et al. 2021b, A&A, 656, A70
1997, in ESA SP-1200, The HIPPARCOS and TYCHO Catalogues, ESA (ed.) (Noordwijk: ESA)
Espinoza, N., Brahm, R., Henning, T., et al. 2020, MNRAS, 491, 2982
Espinoza, N., Hartman, J. D., Bakos, G. Á, et al. 2019, AJ, 158, 63
Everhart, E. 1985, in IAU Colloq. 83: Dynamics of Comets: Their Origin and Evolution, ed. A. Carusi & G. B. Valsecchi (Berlin: Springer), 185
Fabrycky, D., & Tremaine, S. 2007, ApJ, 669, 1298
Fabrycky, D. C., Lissauer, J. J., Ragozzine, D., et al. 2014, ApJ, 790, 146
Foreman-Mackey, D. 2016, JOSS, 1, 24
Foreman-Mackey, D. 2018, RNAAS, 2, 31
Foreman-Mackey, D., Agol, E., Ambikasaran, S., & Angus, R. 2017a, AJ, 154, 220
Foreman-Mackey, D., Agol, E., Angus, R., & Ambikasaran, S. 2017b, AJ, 154, 220
Foreman-Mackey, D., Hogg, D. W., Lang, D., & Goodman, J. 2013, PASP, 125, 306
Foreman-Mackey, D., Luger, R., Agol, E., et al. 2021, JOSS, 6, 3285
Foreman-Mackey, D., Savel, A., Luger, R., et al. 2021, exoplanet-dev/exoplanet v0.5.1, Zenodo, doi:10.5281/zenodo.1998447
Fortney, J. J., Marley, M. S., & Barnes, J. W. 2007, ApJ, 659, 1661
Francesco, A., Mario, D., Li, Z., & Alessandro, S. 2022, RNAAS, 6, 28
Gaia Collaboration, Brown, A. G. A., Vallenari, A., et al. 2018, A&A, 616, A1
Gaia Collaboration, Brown, A. G. A., Vallenari, A., et al. 2021, A&A, 649, A1
Gaia Collaboration, Prusti, T., de Bruijne, J. H. J., et al. 2016, A&A, 595, A1
Gill, S., Wheatley, P. J., Cooke, B. F., et al. 2020, ApJL, 898, L11
Gladman, B. 1993, Icar, 106, 247
Goldreich, P., & Tremaine, S. 1979, ApJ, 233, 857
Guerrero, N. M., Seager, S., Huang, C. X., et al. 2021, ApJS, 254, 39
Guillot, T., Abe, L., Agabi, A., et al. 2015, AN, 336, 638
Guillot, T., Fletcher, L. N., Helled, R., et al. 2022, arXiv:2205.04100
Guillot, T., & Morel, P. 1995, A&AS, 109, 109
Guillot, T., Santos, N. C., Pont, F., et al. 2006, A&A, 453, L21
Hellier, C., Anderson, D. R., Collier Cameron, A., et al. 2017, MNRAS, 465, 3693
Hippke, M., David, T. J., Mulders, G. D., & Heller, R. 2019, AJ, 158, 143
Hippke, M., & Heller, R. 2019, A&A, 623, A39
Holman, M. J., Fabrycky, D. C., Ragozzine, D., et al. 2010, Sci, 330, 51
Huang, C., Wu, Y., & Triaud, A. H. M. J. 2016, ApJ, 825, 98
Ida, S., & Lin, D. N. C. 2010, ApJ, 719, 810
Jenkins, J. M., Twicken, J. D., McCauliff, S., et al. 2016, Proc. SPIE, 9913, 99133E
Jordán, A., Brahm, R., Espinoza, N., et al. 2020, AJ, 159, 145
Kanagawa, K. D., Tanaka, H., & Szuszkiewicz, E. 2018, ApJ, 861, 140
Kaufer, A., Stahl, O., Tubbesing, S., et al. 1999, Msngr, 95, 8
Kipping, D. M. 2013, MNRAS, 435, 2152
Kley, W., & Nelson, R. P. 2012, ARA&A, 50, 211
Kossakowski, D., Espinoza, N., Brahm, R., et al. 2019, MNRAS, 490, 1094
Kreidberg, L. 2015, PASP, 127, 1161
Kumar, R., Carroll, C., Hartikainen, A., & Martin, O. A. 2019, JOSS, 4, 1143
Laskar, J., & Petit, A. C. 2017, A&A, 605, A72
Lee, M. H. 2004, ApJ, 611, 517
Levison, H. F., Kretke, K. A., & Duncan, M. J. 2015, Natur, 524, 322
Lightkurve Collaboration, Cardoso, J. V. D. M., Hedges, C., et al. 2018, Lightkurve: Kepler and TESS time series analysis in Python, Astrophysics Source Code Library, ascl:1812.013
Lin, D. N. C., & Papaloizou, J. 1979, MNRAS, 186, 799
Lin, D. N. C., & Papaloizou, J. 1986, ApJ, 309, 846
Lissauer, J. J., Ragozzine, D., Fabrycky, D. C., et al. 2011, ApJS, 197, 8
Lithwick, Y., Xie, J., & Wu, Y. 2012, ApJ, 761, 122
Luque, R., Pallé, E., Kossakowski, D., et al. 2019, A&A, 628, A39
Mandel, K., & Agol, E. 2002, ApJL, 580, L171
Masuda, K. 2014, ApJ, 783, 53
Matsumura, S., Brasser, R., & Ida, S. 2021, A&A, 650, A116

Mékarnia, D., Guillot, T., Rivet, J. P., et al. 2016, MNRAS, 463, 45
Millholland, S., Laughlin, G., Teske, J., et al. 2018, AJ, 155, 106
Mishra, L., Alibert, Y., Leleu, A., et al. 2021, A&A, 656, A74
Nesvorný, D., Kipping, D., Terrell, D., et al. 2013, ApJ, 777, 3
Nesvorný, D., & Vokrouhlický, D. 2016, ApJ, 823, 72
Paardekooper, S. J., Baruteau, C., & Kley, W. 2011, MNRAS, 410, 293
Parmentier, V., Guillot, T., Fortney, J. J., & Marley, M. S. 2015, A&A, 574, A35
Petrovich, C., & Tremaine, S. 2016, ApJ, 829, 132
Rasio, F. A., & Ford, E. B. 1996, Sci, 274, 954
Rein, H., & Liu, S. F. 2012, A&A, 537, A128
Ricker, G. R., Winn, J. N., Vanderspek, R., et al. 2015, JATIS, 1, 014003
Rivera, E. J., Laughlin, G., Butler, R. P., et al. 2010, ApJ, 719, 890
Rubenzahl, R. A., Dai, F., Howard, A. W., et al. 2021, AJ, 161, 119
Salvatier, J., Wiecki, T. V., & Fonnesbeck, C. 2016, PeerJ Computer Science, 2, e55
Santerne, A., Moutou, C., Tsantaki, M., et al. 2016, A&A, 587, A64
Schlecker, M., Kossakowski, D., Brahm, R., et al. 2020, AJ, 160, 275
Schlecker, M., Mordasini, C., Emsenhuber, A., et al. 2021a, A&A, 656, A71
Schlecker, M., Pham, D., Burn, R., et al. 2021b, A&A, 656, A73
Skilling, J. 2004, in AIP Conf. Ser. 735, Bayesian Inference and Maximum Entropy Methods in Science and Engineering, ed. R. Fischer, R. Preuss, & U. V. Toussaint (Melville, NY: AIP), 395
Smith, J. C., Stumpe, M. C., Van Cleve, J. E., et al. 2012, PASP, 124, 1000
Speagle, J. S. 2020, MNRAS, 493, 3132
Steffen, J. H., Fabrycky, D. C., Agol, E., et al. 2013, MNRAS, 428, 1077
Stumpe, M. C., Smith, J. C., Van Cleve, J. E., et al. 2012, PASP, 124, 985
Tan, X., Payne, M. J., Lee, M. H., et al. 2013, ApJ, 777, 101
Tayar, J., Claytor, Z. R., Huber, D., & van Saders, J. 2022, ApJ, 927, 31
Teske, J., Díaz, M. R., Luque, R., et al. 2020, AJ, 160, 96
Theano Development Team 2016, arXiv:1605.02688
Trifonov, T. 2019, The EXO-STRIKER: Transit and radial velocity interactive fitting tool for orbital analysis and N-body simulations, Astrophysics Source Code Library, ascl:1906.004
Trifonov, T., Brahm, R., Espinoza, N., et al. 2021, AJ, 162, 283
Trifonov, T., Kürster, M., Zechmeister, M., et al. 2018, A&A, 609, A117
Trifonov, T., Rybizki, J., & Kürster, M. 2019, A&A, 622, L7
Wang, S., Jones, M., Shporer, A., et al. 2019, AJ, 157, 51
Wisdom, J., & Holman, M. 1991, AJ, 102, 1528